

ISSN 1450-7404

Journal of Research in Physics

Volume 33
Number 1
2009



DEPARTMENT OF PHYSICS

Faculty of Sciences
University of Novi Sad - Novi Sad - Serbia

Journal of Research in Physics

Editor
Mario Škrinjar

Editor-in-Chief
Ištvan Bikit

INTERNATIONAL EDITORIAL BOARD

Lajos Bata

Research Institute for
Solid State Physics
Budapest, Hungary

Nikos Flytzanis

Physics Department
University of Crete
Iraklion, Greece

Kazuo Tanaka

Institute of Laser
Engineering
Osaka, Japan

Emilio Marquez Navarro

Departamento de Física
de la Materia Condensada
Universidad de Cadiz
Cadiz, Spain

Padma Shukla

Ruhr - Universität Bochum
Bochum, Germany

Stevica Djurović

Svetlana Lukić
Zoran Mijatović
Jaroslav Slivka
Jovan Šetrajić
Department of Physics
University of Novi Sad
Novi Sad
Serbia

Ivan Aničin

Jaroslav Labat

Jagoš Purić

Physical Faculty
University of Belgrade
Belgrade
Serbia

Milan Dimitrijević

Astronomical Observatory
Belgrade
Serbia

Zoran Popović

Institute of Physics
Belgrade
Serbia

Published by: Department of Physics, Faculty of Sciences, University of Novi Sad,
Trg Dositeja Obradovića 4, 21000 Novi Sad, Serbia

Phone: +381-21-455318

Fax: +381-21-459367

E-mail: jresphys@df.uns.ac.rs

<http://www.df.uns.ac.rs>

Origination of the Davydov's Soliton in the Linear Polymer Chain

Dragan R. Todorović

*Faculty of Science, University of Kragujevac,
Radoja Domanovića 12, 34000 Kragujevac, Serbia*

Received: June 16, 2009

Abstract

In this paper the origination of the Davydov's soliton in the linear polymer chain, both ideal and with a single impurity, is considered applying numerical analysis to discrete equations. It is demonstrated explicitly that the soliton velocity is inversely proportional to the soliton amplitude. The different soliton behavior is observed after the exciton creation at the beginning and in the bulk of the linear polymer chain.

Key words: Davydov's soliton, linear polymer chain, impurity

1. Introduction

It is the fact that the Davydov's soliton model [1] was a subject of intensive theoretical investigations during the last three decades. Its importance lies in the attempts to understand and describe energy transport process in α -helix proteins and peptides. The main idea in the Davydov model is the coupling between exciton and phonon of the polymer chain. Due to the nonlinear and strong exciton-phonon interaction, auto-localized excitations solitons appear in the system [2,3].

Davydov's model is of methodological importance: it aims to explain the localization and the transport of energy in α -helix proteins. Numerous scientists have investigated the above idea: the soliton mechanism of the energy transport in the protein molecules (cf. [4-7] and refs. therein) including the foundation and accuracy of the theory, the quantum and classical properties and the thermal stability and lifetime of the Davydov's soliton. Some recent studies throw new light on the topic [8-15].

However, in the majority of the papers, Davydov's soliton is created "artificially". All existing numerical analyses and inverse scattering method studies of launching the soliton were based on the assumption that the soliton is already existing in the chain [4].

Continual approximation in the Davydov's soliton model (under condition when the soliton appears in the linear polymer chain) always gives fixed shape of the soliton, with well-known velocity (analytic solution of the differential equation (11-13)).

The dynamic equations of motion (9) and (10) give possibility for the numerical simulation of the soliton creation, its time evaluation and propagation along the linear polymer chain.

The aim of this paper is to show, using the numerical analysis of equations (9) and (10), that the soliton features and behavior in a linear polymer chain depend on the position where it is created: at the beginning or in the “bulk” of the chain.

The paper is organized as follows: Section 2 presents the model Hamiltonian of the ideal polymer chain and the polymer chain with a single impurity at arbitrary site. Basic discrete equations for exciton and phonon amplitudes are formulated in Section 3. Next section describes the elements of the calculation procedure for solving the system of coupled difference equations. The results of the numerical analysis, both for ideal chain and single impurity are given in Section 5. All calculations were performed with the set of parameters which can be found in the relevant literature. The results are summarized in a concise Conclusion.

2. The system Hamiltonian

2.1. The ideal polymer chain

Our starting point is the standard Davydov’s Hamiltonian for the ideal linear polymer chain

$$\hat{H}_D = \hat{H}_{ex} + \hat{H}_{ph} + \hat{H}_{int}. \quad (1)$$

The term \hat{H}_{ex} , represents the monomer amide-I quantum excitations. It will be considered, in accordance with Davydov’s approach, as the Frenkel’s exciton [3,4,16] in the so-called two level approximation, i.e. only the ground and the first excited levels are taken into account. The higher excited levels are supposed to be sufficiently far away from the first excited level [3].

The term \hat{H}_{ph} describes the vibration of the monomer units while the term \hat{H}_{int} describes the exciton-phonon interaction.

The Hamiltonian \hat{H}_{ex} , involving the nearest neighbors approximation, has the following form:

$$\hat{H}_{ex} = \sum_n \left[E_0 \hat{B}_n^+ \hat{B}_n - J \left(\hat{B}_n^+ \hat{B}_{n+1} + \hat{B}_{n+1}^+ \hat{B}_n \right) \right]. \quad (2)$$

In equation (2) \hat{B}_n^+ and \hat{B}_n are the Bose operators that create and annihilate the excitation on the n -th chain site. J represents resonance energy of dipole-dipole interactions between neighboring peptide groups. E_0 represents the excitation energy of each monomer unit renormalized due to the resonant interaction between the neighboring monomer units.

The phonon Hamiltonian \hat{H}_{ph} corresponding to the displacement of monomer units from their equilibrium position has the following form:

$$\hat{H}_{ph} = \frac{1}{2} \sum_n \left[\frac{1}{m} \hat{p}_n^2 + k (\hat{u}_n - \hat{u}_{n-1})^2 \right], \quad (3)$$

where m is the mass of the displaced monomer unit; \hat{p}_n is the momentum operator canonically conjugated to the displacement operator \hat{u}_n of the n -th monomer unit, k is the lattice elasticity coefficient.

Hamiltonian \hat{H}_{int} of the exciton-lattice interaction is of the form

$$\hat{H}_{int} = \chi \sum_n \hat{B}_n^+ \hat{B}_n (\hat{u}_{n+1} - \hat{u}_{n-1}). \quad (4)$$

where χ is the exciton-phonon coupling parameter.

2.1.1 Dynamic equations of the solitary waves in the ideal linear polymer chain

As is known from the theory of Davydov's model, in the case of strong exciton-lattice coupling and small longitudinal elasticity coefficient ("soft" polymer chain), the solitonic excitations could arise in the system. The calculation procedure given here is the derivation of basic dynamical equations of the theory of Davydov's model [17-20], and therefore they will be given only briefly.

The first step is to write down the averaged equation of motion of the lattice and the time-dependent Schrödinger equation of the whole system, using the system Hamiltonian \hat{H}_D and the following single-quasi-particle wave function

$$|\Psi(t)\rangle = \sum_n \left[A_n(t) e^{-\frac{i}{\hbar} \hat{S}(t)} B_n^+ |0\rangle \right], \quad \hat{S}(t) = \sum_n [\alpha_n(t) \hat{p}_n - \pi_n(t) \hat{u}_n], \quad (5)$$

where $|0\rangle$ is the vacuum state function, i.e. $|0\rangle = |0\rangle_{ex} \otimes |0\rangle_{ph}$. Unitary operator $\exp\left[-\frac{i}{\hbar} \hat{S}(t)\right]$ is usually used in the theory of the lattice vibrations in the presence of the external forces; $\alpha_n(t)$ and $\pi_n(t)$ are the coherent state representations of \hat{u}_n and \hat{p}_n , while $A_n(t)$ determines the probability of creating the exciton on the lattice site n , which means that

$$\sum_n |A_n(t)|^2 = 1. \quad (6)$$

The complex function $A_n(t)$ and the real functions $\alpha_n(t)$ and $\pi_n(t)$ are found by the variation method from the condition for the minimum of the functional

$$\Phi(\{A_n, \alpha_n, \pi_n\}) \equiv \langle \Psi(t) | \hat{H}_D | \Psi(t) \rangle. \quad (7)$$

The coherent state representation of the operators \hat{u}_n and \hat{p}_n is given by

$$\alpha_n(t) = \langle \Psi(t) | \hat{u}_n | \Psi(t) \rangle; \quad \pi_n(t) = \langle \Psi(t) | \hat{p}_n | \Psi(t) \rangle. \quad (8)$$

The condition for the minimum of the functional (7) results in the system of coupled equations

$$i\hbar \frac{\partial A_n}{\partial t} = [\Lambda + \chi(\alpha_{n+1} - \alpha_{n-1})] A_n - J(A_{n+1} + A_{n-1} - 2A_n), \quad (9)$$

$$m \frac{d^2 \alpha_n}{dt^2} = k[\alpha_{n+1} + \alpha_{n-1} - 2\alpha_n] + \chi \left[|A_{n+1}|^2 - |A_{n-1}|^2 \right], \quad (10)$$

where $\Lambda = E_0 + E_{ph}$ and E_{ph} represents lattice phonon energy, i.e.

$$E_{ph} = \frac{1}{2} \sum_n \left[\frac{1}{m} \pi_n^2 + k(\alpha_n - \alpha_{n-1})^2 \right].$$

Since our main aim is to perform the numerical analysis of the last two equations, we shall only quote for the sake of comparison, the equations in the continuum approximation [2]

$$\left(\frac{\partial^2}{\partial t^2} - v_0^2 \frac{\partial^2}{\partial x^2} \right) \rho(x, t) + \frac{2a\chi}{m} \frac{\partial^2}{\partial x^2} |A(x, t)|^2 = 0, \quad (11)$$

$$\left[i\hbar \frac{\partial}{\partial t} - \Lambda + Ja^2 \frac{\partial^2}{\partial x^2} + 2a\chi\rho(x,t) \right] A(x,t) = 0, \quad \rho(x,t) = -\frac{\partial\alpha(x,t)}{\partial x}. \quad (12)$$

It is possible to find the particular, bell-shaped solution of Eqs. (11–12) (Davydov soliton) propagating along the chain with velocity v_0 , only if we assume stationary solutions of the form

$$\rho(x,t) = \rho\left(\frac{x}{a} - \frac{v_0}{a}t\right); \quad A(x,t) = \Phi\left(\frac{x}{a} - \frac{v_0}{a}t\right)e^{i\gamma(x,t)}. \quad (13)$$

It is clear that due to this choice the problem of initial conditions is not a relevant one in the continuum version of Davydov’s model.

2.2. Nonideal polymer chain

Davydov’s model treat the α -helix protein, made of identical monomer units, which is not true in reality. Real α -helix protein is composed of the different monomer units. Namely, the proteins are the macromolecules composed of 20 different amino acids.

We take into account the above complexity of the protein structure and consider a relatively simple model of nonideal linear polymer chain, that is, an ideal polymer chain with the one implanted different monomer unit, which is treated as “impurity”. Placing impurity in the ideal linear polymer chain disturbs the translational invariance. The disturbance of the structure caused by the impurity, is considered as a particular perturbation of the Hamiltonian of the ideal chain. This approach, which is also numerically verified, allows adapting the theoretical method used for analysis of the ideal chain and applying it easily to a nonideal chain with impurity [21].

The particular manner in which we include the perturbation caused by the impurity, affects some of the previously considered Hamiltonian terms. Namely, although the chain has the impurity, the Hamiltonian \hat{H}_D (which is in fact the Hamiltonian of the ideal Davydov’s model) describes an ideal polymer chain with no impurities. As we have the chain with impurity at some place in the chain, this means that some nonexisting terms have been added to \hat{H}_D and therefore these terms must be extracted and the terms corresponding to the impurities included too. In order to solve this problem, we follow the usual theory of a single impurity in the crystal lattice, where it is taken that the presence of impurity on some lattice site is equivalent to the presence of a local potential on that site. In other words, this means that impurity affects the coupling constant and the other relevant parameters mainly near the impurity position. Consequently \hat{H}_{res} could be extracted from the Hamiltonian \hat{H}_D in which the constants E_0 , J , k , χ have been renormalized in an appropriate manner. However, the corrections of all of these constants need not be considered because some of them are physically negligible. We explicitly take into account the constant E_0 and the constant of the resonance energy dipole-dipole interaction J , due to their expected dominance in the soliton propagation. These quantities should be substituted by the new ones $E_0 + \tilde{\Delta}Y(na)$, and $J + \tilde{J}Y(na)$, where $Y(na) \equiv Y_n$ is the function of the lattice position “vector” na which has the following form

$$Y_n = e^{-\beta a(n-n_0)^2}, \quad (14)$$

that has its maximum at n_0 , the lattice site where the impurity is placed. As can be seen, Y_n is chosen to be sufficiently fast decreasing (exponentially). Constant β depends on the potential induced by the impurity effects and it will be obtained from the physical condition that the impurity affects only several nearest neighbors.

Taking into account the previous facts, which indicate that only the exciton parameters are corrected, it is easy to show that the exciton Hamiltonian of the nonideal chain can be expressed as a sum of the aforementioned exciton Hamiltonian of the ideal chain \hat{H}_{ex} and Hamiltonian of the residue \hat{H}_{res} , which is of the form

$$\hat{H}_{res} = \sum_n \tilde{\Delta} Y_n \hat{B}_n^+ \hat{B}_n - \sum_n \tilde{J} Y_n \left(\hat{B}_n^+ \hat{B}_{n+1} + \hat{B}_{n+1}^+ \hat{B}_n \right). \quad (15)$$

The nonzero terms in the above sums are only due to the monomer units in which the impurities are present.

Finally, the Hamiltonian of the nonideal polymer chain is of the form

$$\hat{H}_{NI} = \hat{H}_D + \hat{H}_{res}.$$

3. Dynamic equations of the solitary waves in the nonideal linear polymer chain

The calculation procedure given here is the derivation of basic dynamical equations of the theory of Davydov's model. The only difference in this case, which does not change the calculation procedure, is the presence of \hat{H}_{res} in the system Hamiltonian.

Instead of equation (9) and (10) we obtain

$$\begin{aligned} \frac{d^2 \alpha_n}{dt^2} = & k [\alpha_{n+1} + \alpha_{n-1} - 2\alpha_n] + \chi_1 \left[|A_{n+1}|^2 - |A_{n-1}|^2 \right] \\ & + \chi_2 \left[A_n^* (A_{n+1} - A_{n-1}) + (A_{n+1}^* - A_{n-1}^*) A_n \right]. \end{aligned} \quad (16)$$

On the other hand, by substituting $|\Psi(t)\rangle$ (Eq. 5) into the time-dependent Schrödinger equation, where the total system Hamiltonian \hat{H}_{NI} has been used, we have derived that:

$$\begin{aligned} i\hbar \frac{\partial A_n}{\partial t} = & [\Lambda + \varepsilon Y_n + \chi(\alpha_{n+1} - \alpha_{n-1})] A_n \\ & - (J + \tilde{J} Y_n)(A_{n+1} + A_{n-1} - 2A_n), \end{aligned} \quad (17)$$

where $\varepsilon = \tilde{\Delta} - 2\tilde{J}$.

When $\tilde{\Delta} = 0$ and $\tilde{J} = 0$ equations (16) and (17) describe the dynamics of the ideal linear polymer chain.

4. Procedure and results of the numerical analysis

Equations (9) and (10), i.e. (16) and (17), which determine the dynamics of the considered linear polymer chain (ideal and nonideal), has been analyzed numerically in [21].

4.1. Procedure

Method Runge-Kutta 4-th order is used for numerical solving of equations (9) and (10), i.e. (16) and (17). Programming is realized in Fortran f90 in double precision.

a) Step Runge-Kutta method used in this numerical analysis is chosen to be $h = 5 \cdot 10^{-5}$.

b) Values of the constants used in equations (9) and (10), i.e. (16) and (17) are

1^0 $N = 201$ – number of monomer units in the linear polymer chain (with and without impurity).

2^0 In the unideal linear polymer chain, impurity is placed at the 160-th site.

3^0 $m = 1.9 \cdot 10^{-25}$ kg – monomer unit mass (the mass interval α -amino acids is $(1.17 - 1.91) \cdot 10^{-25}$ kg).

4^0 $k = 19 \frac{\text{N}}{\text{m}}$ – elasticity coefficient [22,23].

5^0 $J = 1.55 \cdot 10^{-22}$ J – the resonance energy of the dipole-dipole interactions between neighboring monomer units. [24-26].

6^0 $\chi = 6.2 \cdot 10^{-11} N = \text{const}$ exciton-phonon interaction [27,28].

c) Initial conditions

1^0 In the case when exciton is created at the beginning of the linear polymer chain, at $t = 0$ we put $A_1(0) = (1, 0)$ and $A_i(0) = (0, 0)$ ($i = 2 \dots N$), i.e. the first monomer unit was excited, while the rest of the monomer units were in the ground state. N denotes the number of monomer units in the considered linear polymer chain.

2^0 In the case when exciton is created at the bulk of the linear polymer chain, at $t = 0$ we put $A_{N_0}(0) = (1, 0)$ and $A_i(0) = (0, 0)$ ($i = 1 \dots N$, $i \neq N_0$), i.e. the monomer unit placed at N_0 was excited, while the rest of the monomer units were in the ground state.

3^0 $\alpha_i(0) = 0$ and $\pi_i(0) = 0$ ($i = 1, \dots, N$), i.e. all monomer units of the linear polymer chain are in the equilibrium position.

A simple unitary transformation of the amplitude $A_n(t)$ eliminates the constant term in equations (9) and (19).

5. Results of the numerical analysis

5.1. The ideal linear polymer chain

Fig. 1 shows the soliton propagation. Exciton is created at the beginning of the linear polymer chain, i.e. at the first monomer unit.

Fig. 2 shows the case when exciton is created in the middle of the linear polymer chain at $N_0 = 101$ -th monomer unit. As we can see from the numerical analysis of equations (9) and (10) (different pictures), of the soliton propagation in the ideal linear polymer chain, is obtained depending on where the exciton is created: a) at the origin of the linear polymer chain (Figure 1) or b) in the bulk of the linear polymer chain (Figure 2)

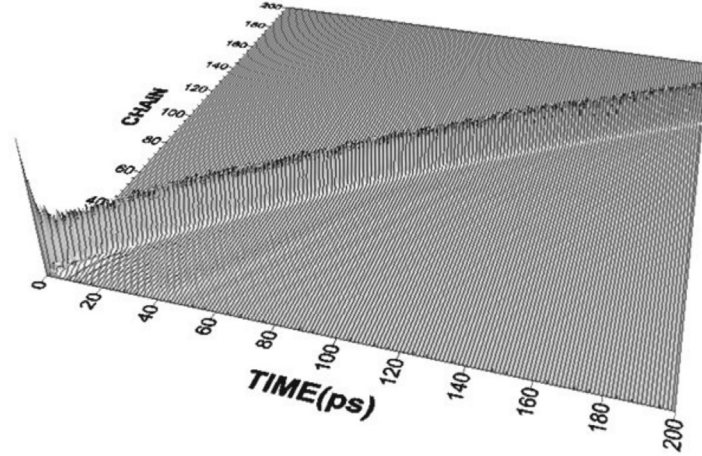


Figure 1. Propagation of the soliton in the ideal linear polymer chain. Exciton is created at the origin of the chain.

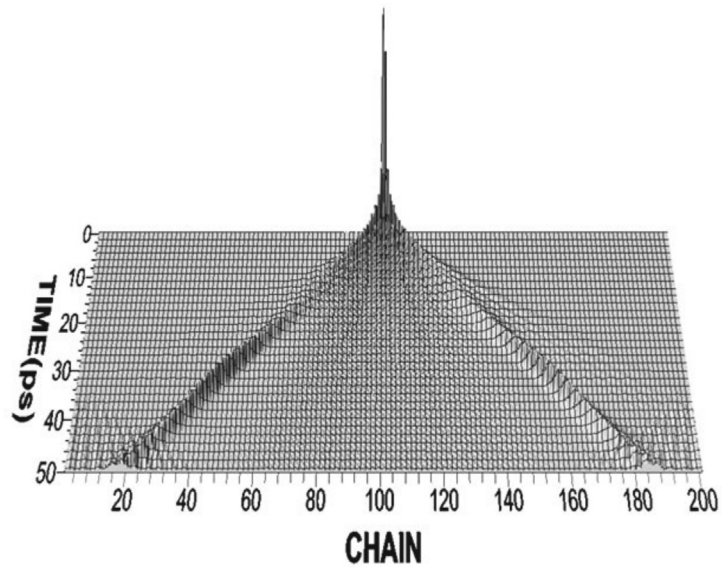


Figure 2. Propagation of the soliton in the ideal linear polymer chain. Exciton is created in the middle of the chain.

In the continual approximation of Davydov's model, the soliton has fixed shape and velocity and soliton is always created. If exciton is created in the bulk of the linear polymer chain particular solution of the equations (14) and (15) has two particular solutions, one of the type $\rho(\frac{x}{a} - \frac{v_0}{a}t)$ and the other one $\rho(\frac{x}{a} + \frac{v_0}{a}t)$. This is difficult to identify analytically with the present initial conditions, while in our numerical analysis of the equations (9) and (10) this result is obtained (Figure 2).

Figure 3 displays comparative soliton shapes at $t = 50$ ps. Soliton1 is the shape of the soliton wave in the ideal linear polymer chain where exciton is created at the origin of the chain. Soliton2 is the shape of the soliton wave in the ideal linear polymer chain where exciton is created in the middle of the chain. Rough estimate, as we seen from Figure 3 is that the soliton started from middle of the chain is about 1.6 times faster than the soliton started from the origin of the ideal linear polymer chain.

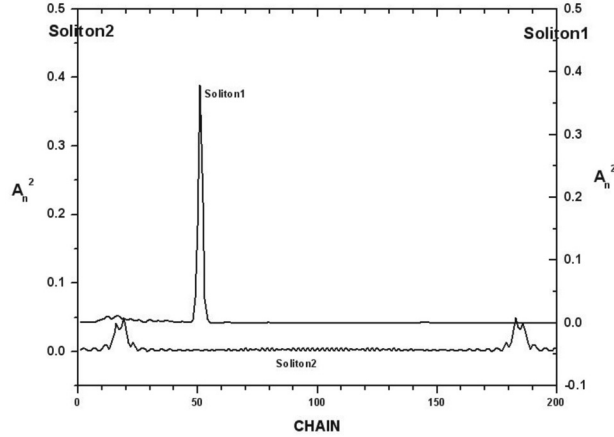


Figure 3. Comparative soliton shapes at $t = 50$ ps in the ideal linear polymer chain. Soliton1 shape of the soliton created at the origin of the chain; Soliton2 shape of the soliton created in the middle of the chain.

The above result was a signal to investigate this behavior more thoroughly. We decided to test the relation between the amplitude and the soliton velocity. Using the chain of 100 monomer units and

Runge-Kutta method step $h = 1 \cdot 10^{-4}$ with all other data as described in Section 4, we obtained the following plot:

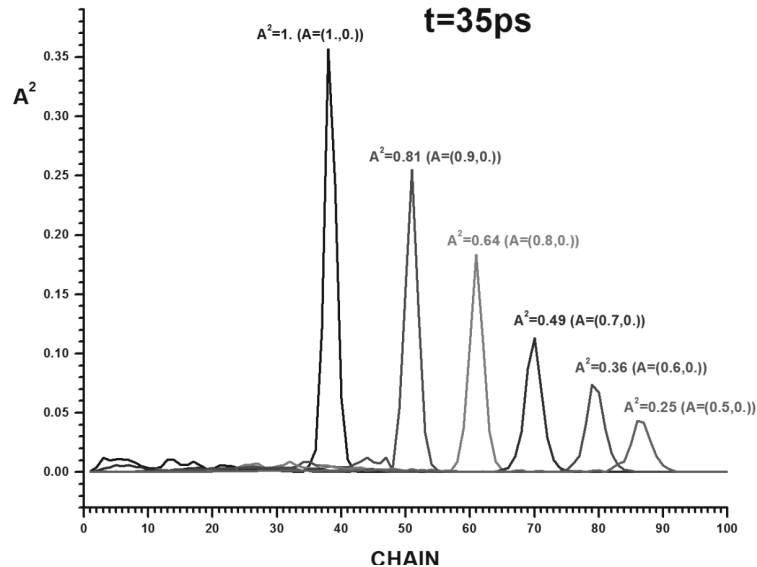


Figure 4. Amplitude square in the linear chain for $t = 35$ ps.

This is even better illustrated by Table 1, which lists the amplitude, amplitude square and the lattice site (N_{\max}) where the wave has the maximum for $t = 35$ ps.

Table 1.

A	A^2	N_{\max}
(0.5,0.0)	0.25	86
(0.6,0.0)	0.36	79
(0.7,0.0)	0.49	70
(0.8,0.0)	0.64	61
(0.9,0.0)	0.81	51
(1.0,0.0)	1.0	38

This allowed us to plot the absolute value of the amplitude $|A|$ and soliton velocity for $t = 35$ ps.

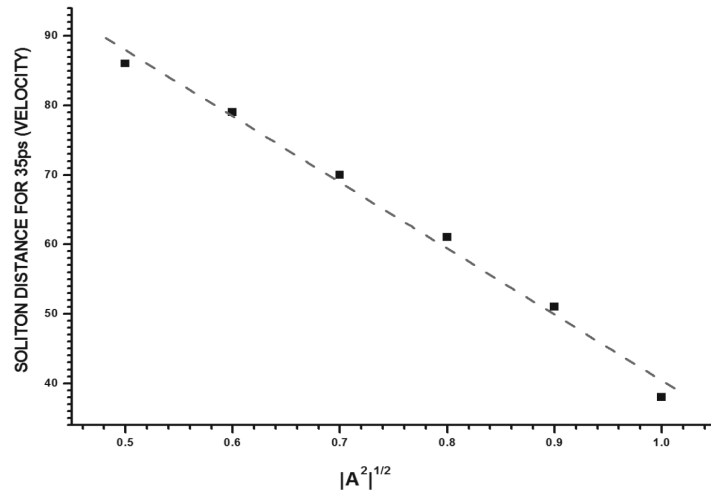


Figure 5. The relation between absolute value of the amplitude and soliton velocity for $t = 35$ ps.

Dashed curve obviously corresponds to the linear fit, and this is essentially a completely new result since till now this was just a conjecture for Davydov's solitons, i.e. the soliton velocity decreasing with amplitude.

5.2. The nonideal linear polymer chain

Special behavior of the soliton propagation, in the linear polymer chain with impurity, is investigated applying numerical analysis. The impurity, placed at the 160-th site ($\Delta = 0.3 \cdot 10^{-22} J$) in the linear polymer chain, acts as the energy barrier to the soliton propagation (Figure 4). If the soliton is created at the origin, it is completely reflected by the barrier.

Soliton propagation in the linear chain with impurity is investigated applying numerical analysis. The impurity placed at the 160-th site acts as an energy barrier ($\Delta = 0.3 \cdot 10^{-22} J$) for the soliton propagating. If the soliton is created at the beginning of the chain, it is

completely reflected by the barrier (Figure 6).

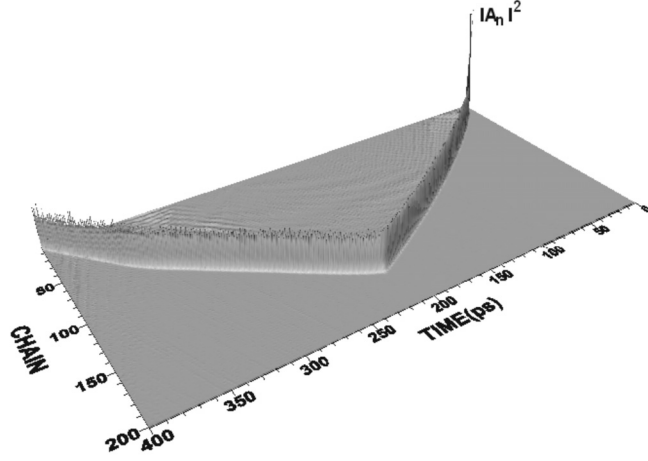


Figure 6. Soliton propagation in the linear polymer chain with the impurity placed at the 160-th site. Impurity acts on the soliton as the energy barrier ($\tilde{\Delta} = 0.3 \cdot 10^{-22} J$). Exciton is created at the origin of the chain.

If the soliton is created in the “bulk” under the same conditions, however, two soliton waves appear in the linear polymer chain, propagating in the opposite directions (Figure 7).

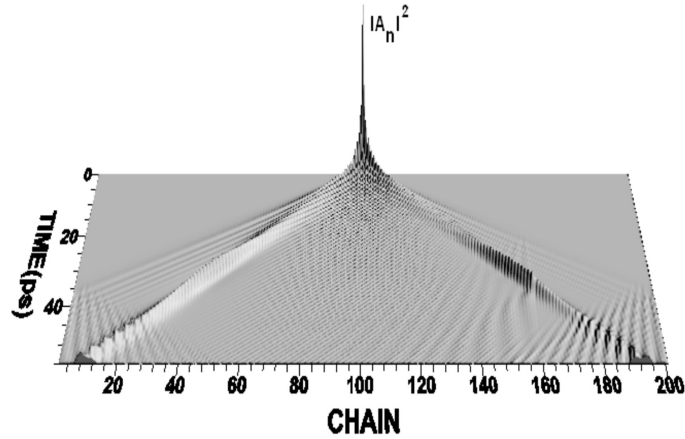


Figure 7. Soliton propagation in the linear polymer chain with the impurity placed at the 160-th site. Energy barrier has the value ($\tilde{\Delta} = 0.3 \cdot 10^{-22} J$).

As shown previously, since total energy splits between two solitons, the amplitude of each branch is lower, so its velocity increases and enhances its delocalization (with the shape profile broadening). This allows the soliton to pass the barrier more easily (quasi-classical analogue of tunneling). However, this passage has the consequence of diminishing the amplitude behind the barrier.

6. Conclusion

Numerical results just presented indicate that the shape and velocity of the soliton wave formed in the chain with impurity, substantially depend on the position where the soliton is created. If the soliton in the numerical simulation is “created” at the beginning of the chain, a single soliton wave is formed propagating in a single direction along the chain. However, if the soliton is formed within the “bulk” of the chain, two waves are formed, propagating in both directions. It is interesting that the square of the amplitude (sum of the areas below the bell shaped curves) is equal to the area of the single soliton formed at the origin. This is a consequence of the normalizing condition for the wave function. As for the influence of the impurity to the soliton propagation, the magnitude of the barrier can be chosen in such a manner that the soliton “smoothly” passes the barrier. It was demonstrated that the soliton velocity is inversely proportional to the absolute value of the soliton amplitude. This is an important result since similar conclusion can not be drawn from the continuum theory. This result implies that the velocity increase causes the decrease of effective soliton mass, i.e. soliton becomes more delocalized (the shape profile broadens) and more easily tunnels through the impurity energy barrier. This is compatible with the fact that we are dealing with a conservative system.

Acknowledgments

The work is financially supported by Ministry of Science and Technological Development. Contract No. 141016.

References

- [1] A.S. Davydov, N.I. Kislukha, *Phys. Stat Sol. (b)* **59**, 465 (1973).
- [2] A.S. Davydov, *Theory of Molecular Excitons*, Plenum Press, New York (1971).
- [3] A.S. Davydov, *Biology and Quantum Mechanics*, Pergamon Press, New York, (1982).
- [4] A. Scott, *Physics Reports* **217(1)**, 1 (1992).
- [5] Pang Xiao Feng, *Phys. Rev. E* **62**, 6989 (2003).
- [6] Pang Xiao-feng, *Eur. Phys. J. B* **19**, 297 (2001).
- [7] S. Gheorghiu-Svirschevski, *Phys. Rev. E* **64**, 051907 (2001).
- [8] Y. Xiao, *Phys. Lett. A* **243**, 174 (1998).
- [9] Lj.D. Mašković, B.S. Tošić, R. Maksimović, *Physica D* **113**, 293 (1998).
- [10] B. Tan , J.P. Boyd, *Phys. Lett. A* **240**, 282 (1998).
- [11] M Daniel, M.M. Latha, *Physica A* **298**, 351 (2001).
- [12] K.T. Stoychev, M.T. Primatarowa, and R.S. Kamburova, *Phys. Rev. E* **70**, 06662 (2004).

-
- [13] M.T. Primatarowa, K.T. Stoychev, and R.S. Kamburova, *Phys. Rev. E* **72**, 036608 (2005).
- [14] K.T. Stoychev, M.T. Primatarowa, and R.S. Kamburova, *Phys. Rev. E* **73**, 066611 (2006).
- [15] Y. Zolotaruk, J.C. Eilbeck, *Phys. Rev. B* **63**, 054302 (2001).
- [16] V.M. Agranovich and M.D. Galanin, *Electronic Energy Transfer in Condensed Matter*, North-Holland Publ. Co., New York, (1982).
- [17] S. Takeno, *Prog. Theor. Phys.* **71**, 395 (1984); *J. Phys. Soc. Jpn.* **59**, 3127 (1991).
- [18] S. Takeno, *Prog. Theor. Phys.* **73**, 853 (1985).
- [19] S. Takeno, *J. Phys. Soc. Jpn.* **59**, 3127 (1990).
- [20] Lj. Ristovski, D. Todorović, G. Davidović and B. Stojković, *Z. Phys. B* **78**, 265 (1990).
- [21] K. Itoh and T. Shimanouchi, *J. Mol. Spectr.* **42**, 86 (1972).
- [22] L.R. LaFara, *Computer Methods for Science and Engineering*, Intertext, Aulesbury (1973).
- [23] V.A. Kuprievich and Z.G. Kudritskaya, Technical Report ITP-82-64E, Institute for Theoretical Physics, Kiev (1982).
- [24] Yu.N. Chirganze and N.A. Nevskaya, *Dokl. Akad. Nauk SSSR* **208**, 447 (1973) (in Russian).
- [25] N.A. Nevskaya and Yu.N. Chirganze, *Bipolymers* **15**, 637 (1976).
- [26] J.C. Elbeck, P.C. Lamdahl and A.C. Scott, *Phys. Rev. B* **30**, 4703 (1984).
- [27] G. Careri, U. Buonatempo, F. Galluzzi, A.C. Scott, E. Gratton and E. Shymasunder, *Phys. Rev. B* **30**, 4689 (1984).
- [28] P.L. Christiansen and A.C. Scott (Ed.), *Davydov's Soliton Revisited*, Plenum Press Publishing Co., New York (1990).

Magnetic Excitations of Ferromagnetic Semiconductor Superlattices

M. Pavkov-Hrvojević, M. Pantić, S. Radošević, M. Rutonjski and D. Kapor
Department of Physics, Faculty of Natural Sciences, University of Novi Sad, Serbia

Received: October 27, 2009

Abstract

Bulk and surface magnetic excitations of ferromagnetic semiconductor (FMS's) superlattices are analyzed using transfer matrix method, developed in our previous paper. Results are discussed in the narrow-band limit. The spin-wave frequencies for a semi-infinite narrow-band semiconductor are analyzed in the low-frequency, as well as in the high-frequency region. Energies of both bulk and localized excitations are compared with the results of Green functions formalism. Numerical results are discussed and illustrated.

Key words: ferromagnetic semiconductors, magnetic superlattice, surface magnetic excitations, transfer matrix method

1. Introduction

Ferromagnetic semiconductors (FMS's), have been the subject of intense study prompted by their fundamental scientific interest and the promise that their compatibility with semiconductor technology may lead to novel spintronic applications [1,2]. However, our understanding of the fundamental magnetic excitations in these materials is still far from being complete.

The problem of calculating magnetic excitations in FMS's is intimately related to the exchange interaction between the localized and itinerant spins [1],[3]-[5]. Theoretical calculations of magnetic excitations in infinitely extended FMS's were obtained already applying the *s-d* (or *s-f*) model [6]-[8]. It has been shown that besides usual "acoustic" spin-wave branches, there are higher frequency (or "optical") branches. Different techniques are used to calculate bulk and surface magnetic spectra for semi-infinite FMS's [9]-[11]. Some magnetic properties of thin films containing itinerant electrons interacting with localized spins are considered as well [12].

In this paper we propose a transfer matrix method, developed in our previous paper [13], which introduces large simplifications in the analysis of elementary excitations of FMS's superlattices. All the calculations are done in the narrow band limit, with $W \ll DS$ where W is the conduction bandwidth, D is the contact interaction energy, and S is the spin of the localized electrons.

The structure of the paper is as follows: in Sec. 2 we formulate the model and demonstrate the transfer matrix procedure through a simple model for an infinite, i.e.

ideal, superlattice. A general solution of the problem is rather difficult analytically, so we demonstrate a special case of narrow-band semiconductors (such as the chromium spinels). Further on, we study semi-infinite superlattice. Some numerical results of the surface and bulk spin-wave spectrum of superlattice the with motive which consists of one plane are presented and compared with the results of Gopalan and Cottam [9]. We study more complicated superlattices, as well as film made of superlattice. Results are analyzed numerically in dependence of the parameters of the system, they are summarized in Sec. 3.

2. Model and transfer-matrix formalism

We will consider infinite FMS's superlattice described by the s - d (or s - f) interaction model. The superlattice is built of the $y - z$ planes which are ferromagnetically ordered and the exchange between the spins within the plane will be denoted by $I > 0$ with an additional subscript.

The motive, or unit cell, i.e. the magnetic structure that repeats itself along x direction, consists of N planes which also interact ferromagnetically. The interaction between the spins belonging to neighboring planes will be denoted by $J > 0$, with the corresponding subscript. The position of an ion is given by $\vec{n} = \vec{\rho} + [mL + (n - 1)a]\vec{e}_x$. Here $\vec{\rho}$ is a two-dimensional vector describing the position within the plane; a is the lattice constant; $L = Na$ is the cell dimension along the x -axis, while m enumerates the cells.

The Hamiltonian of the system is expressed as the sum of three terms:

$$H = H_M + H_E + H_{ME}. \quad (1)$$

H_M is the Heisenberg Hamiltonian for the localized spins (of d or f type) :

$$\begin{aligned} H_M = & -\frac{1}{2} \sum_m \sum_{n=1}^N I_n \sum_{\vec{\rho}} \sum_{\vec{\delta}_{\parallel}} \left\{ \frac{1}{2} \left[\hat{S}_{m\vec{\rho}}^+(n) \hat{S}_{m\vec{\rho}+\vec{\delta}_{\parallel}}^-(n) + H.c. \right] + \hat{S}_{m\vec{\rho}}^z(n) \hat{S}_{m\vec{\rho}+\vec{\delta}_{\parallel}}^z(n) \right\} - \\ & - \sum_m \left\{ \sum_{n=1}^{N-1} J_{n,n+1} \sum_{\vec{\rho}} \left[\frac{1}{2} \left(\hat{S}_{m\vec{\rho}}^+(n) \hat{S}_{m\vec{\rho}}^-(n+1) + \hat{S}_{m\vec{\rho}}^-(n) \hat{S}_{m\vec{\rho}}^+(n+1) \right) + \right. \right. \\ & \left. \left. + \hat{S}_{m\vec{\rho}}^z(n) \hat{S}_{m\vec{\rho}}^z(n+1) \right] + \frac{1}{2} J_{N1} \left[\frac{1}{2} \left(\hat{S}_{m\vec{\rho}}^+(N) \hat{S}_{m+1\vec{\rho}}^-(1) + \hat{S}_{m-1\vec{\rho}}^+(N) \hat{S}_{m\vec{\rho}}^-(1) \right) + \right. \right. \\ & \left. \left. + H.c. + \hat{S}_{m\vec{\rho}}^z(N) \hat{S}_{m+1\vec{\rho}}^z(1) + \hat{S}_{m-1\vec{\rho}}^z(N) \hat{S}_{m\vec{\rho}}^z(1) \right] \right\} - g\mu_B H_0 \sum_{m,\vec{\rho}} \sum_{n=1}^N \hat{S}_{m\vec{\rho}}^z(n) \quad (2) \end{aligned}$$

here $S_{m\vec{\rho}}(n)$ denotes the spin of the ion in the n th plane within the m th cell, and the position within the plane is specified by $\vec{\rho}$. The first term describing the intra-plane interaction also includes the summation over nearest neighbors within the plane whose positions are designated by $\vec{\delta}_{\parallel}$. The second term of H_M describes inter-plane interaction, where the interactions within the given cell are separated from the ones between the cells.

The last term represents Zeeman energy of localized spins, where H_0 is a static magnetic field applied in the z -direction and g is the Lande factor of the localized electrons. H_E represents the kinetic and Zeeman energy of the conduction (s) electrons:

$$H_E = \sum_{m,n} \sum_{\vec{\rho}, \vec{\delta}_{\parallel}, \sigma} t_n^{\parallel} \hat{a}_{m\vec{\rho}\sigma}^+(n) \hat{a}_{m\vec{\rho}+\vec{\delta}_{\parallel}\sigma}^+(n) + \sum_{m,n} \sum_{\vec{\rho}, \sigma} t_{n,n+1}^{\perp} \hat{a}_{m\vec{\rho}\sigma}^+(n) \hat{a}_{m\vec{\rho}\sigma}^+(n+1) - g_e \mu_B H_0 \sum_{m,n} \sum_{\vec{\rho}} \sigma_{m\vec{\rho}}^z(n). \quad (3)$$

Here t_n^{\parallel} and $t_{n,n+1}^{\perp}$ stand for hopping terms in the plane and between the plane, respectively and g_e is the Lande factor of conduction electrons. The most important term in eq. (1) is s - d (or s - f) interaction Hamiltonian H_{ME} , which couples two subsystems (2) and (3) by an intra-atomic exchange interaction D_n :

$$H_{ME} = - \sum_{m,n} \sum_{\vec{\rho}} D_n \hat{S}_{m\vec{\rho}}^+(n) \cdot \hat{\sigma}_{m\vec{\rho}}^+(n) = - \sum_{m,n} \sum_{\vec{\rho}} D_n \left\{ \frac{1}{2} \left(\hat{S}_{m\vec{\rho}}^+(n) \hat{\sigma}_{m\vec{\rho}}^-(n) + \hat{S}_{m\vec{\rho}}^-(n) \hat{\sigma}_{m\vec{\rho}}^+(n) \right) + \hat{S}_{m\vec{\rho}}^z(n) \hat{\sigma}_{m\vec{\rho}}^z(n) \right\}. \quad (4)$$

The spin operator $\vec{\sigma}_i$ of the conduction electrons at the site i can be expressed as $\hat{\sigma}_i^+ = \hat{a}_{i\uparrow}^+ \hat{a}_{i\downarrow}$, $\hat{\sigma}_i^- = \hat{a}_{i\downarrow}^+ \hat{a}_{i\uparrow}$ and $\hat{\sigma}_i^z = \frac{1}{2} (\hat{a}_{i\uparrow}^+ \hat{a}_{i\uparrow} - \hat{a}_{i\downarrow}^+ \hat{a}_{i\downarrow})$, where $\hat{a}_{i\sigma}^+$ and $\hat{a}_{i\sigma}$ are creation and destruction operators at the site i , respectively and $\sigma = \uparrow$ or \downarrow corresponds to the spin-up and spin-down states.

The general procedure we shall apply is explained in detail in [14], so we shall not repeat all the steps. If the hopping term t is small enough (compared to D), the main effect of the conduction electrons is through the interaction term H_{ME} of eq. (4). In this case, $t = 0$ and it is straightforward to construct the equations of motion for the spin operators $\hat{S}_{m\vec{\rho}}^+(n)$ and $\hat{\sigma}_{m\vec{\rho}}^+(n)$. Further on, we perform two-dimensional in-plane Fourier-transform and linearize the equations using random-phase approximation at $T \ll T_C$, in order to obtain the system for spin-wave amplitudes $u_m(n, \vec{k}_{\parallel})$, where $\vec{k}_{\parallel} = (k_y, k_z)$ is the two-dimensional wave-vector which will be omitted further on. This system has the form:

$$(E - \varepsilon_n) u_m(n) + S_n J_{n,n+1} u_m(n+1) + S_n J_{n,n-1} u_m(n-1) = 0; \quad n = 1, 2, \dots, N. \quad (5)$$

where S_n is the magnitude of the localized spin in the n th plane, $J_{N,N=1} \equiv J_{N,1}$, $S_{N=1} \equiv S_1$,

$$\varepsilon_n = g \mu_B H_0 + D_n s_n + \frac{D_n^2 S_n s_n}{E - g_e \mu_B H_0 - D_n S_n} + 4I_n S_n (1 - \gamma(\vec{k}_{\parallel})) + S_{n+1} J_{n,n+1} + S_{n-1} J_{n,n-1}. \quad (6)$$

s_n is the magnitude of electron's spin in n th plane and $\gamma(\vec{k}_{\parallel}) = \frac{1}{2} (\cos k_y a + \cos k_z a)$.

The above equation can be written as

$$\begin{pmatrix} u_m(n+1) \\ u_m(n) \end{pmatrix} = \hat{M}_n \begin{pmatrix} u_m(n) \\ u_m(n-1) \end{pmatrix}. \quad (7)$$

where the transfer matrix \hat{M}_n is given by:

$$\hat{M}_n = \begin{pmatrix} \frac{\varepsilon_n - E}{S_n J_{n,n+1}} & -\frac{J_{n,n-1}}{J_{n,n+1}} \\ 1 & 0 \end{pmatrix}. \quad (8)$$

Further procedure one can find in our paper [13], so we will just give the equation which determines the bulk energies of the system:

$$2 \cos k_x a = \hat{M}_{11}^n + \hat{M}_{22}^n = \text{Tr} \left\{ \hat{M}^n(E) \right\}, \quad (9)$$

where $\hat{M}^n = \hat{M}_n \hat{M}_{n-1} \cdots \hat{M}_1 \hat{M}_N \hat{M}_{N-1} \cdots \hat{M}_{n+1}$, $N + 1 \equiv 1$. We will present the main results for the case of semi-infinite FMS's superlattice.

2.1. Elementary Excitations in the Semi-Infinite FMS's Superlattice

We will assume here that the semi-infinite superlattice possesses a boundary surface, while it extends infinitely in the opposite direction, occupying the half-space $x \geq 0$. Following our previous paper [13], where we introduced the generalized Ansatz $u_m(n) = u(n)\lambda^{m-1}$, we can use the following expression for the determination of the surface modes:

$$M_0^{21} (\lambda - M_{22}) - M_{21} M_0^{11} = 0, \quad (10)$$

which, when combined with the equation

$$\lambda + \frac{1}{\lambda} = M_{11} + M_{22}, \quad (11)$$

allows the determination of the energies of elementary excitations in the system. $(M)_{ij}$ are the matrix elements of the matrix $\hat{M} = \prod_{n=N}^1 \hat{M}_n$, where N denotes the number of the bulk planes, while $(M_0)^{ij}$ are the matrix elements of the matrix \hat{M}_0 given by:

$$\hat{M}_0 = \begin{pmatrix} 1 & 0 \\ \frac{\Delta \varepsilon_1}{S_1 J_{N1}} & \frac{J_{N01}}{J_{N1}} \end{pmatrix} \hat{M}_S, \quad \Delta \varepsilon_1 = \varepsilon_1 - \varepsilon_1^t. \quad (12)$$

where N_0 denotes the number of the planes in the surface cell (N_0 is not necessarily equal to N) and $\hat{M}_S = \prod_{n=N_0}^1 \hat{M}_n^S$, where

$$\hat{M}_n^S = \begin{pmatrix} \frac{\varepsilon_n^S - E}{S_n J_{n,n+1}^S} & -\frac{J_{n,n-1}^S}{J_{n,n+1}^S} \\ 1 & 0 \end{pmatrix}, \quad n = 2, 3, \dots, N_0. \quad (13)$$

while for $n = 1$ we have:

$$\hat{M}_1^S = \begin{pmatrix} \frac{\varepsilon_1^S - E}{S_1 J_{1,2}^S} & -1 \\ 1 & 0 \end{pmatrix}. \quad (14)$$

We get ε_1 and ε_1^t from eq. (6) for $n = 1$, taking into account that $n-1 \equiv N$ and $n-1 \equiv N_0$, respectively and $\varepsilon_1^S = g\mu_B H_0 + D_1^S s_1^S + \frac{(D_1^S)^2 S_1^S s_1^S}{E - g\mu_B H_0 - D_1^S S_1^S} + 4I_1^S S_1 (1 - \gamma(\vec{k}_{\parallel})) + S_2 J_{12}^S$.

To compare with the work [9], we have studied the simplest case first, when the motive consists of one plane ($N = 1$). Combining eq. (6) and (9), we get the equation for the bulk excitations:

$$E - g\mu_B H_0 - 2SI \left(3 - 2\gamma(\vec{k}_{\parallel}) - \cos k_x a \right) - Ds - \frac{D^2 S s}{E - g_e \mu_B H_0 - DS} = 0. \quad (15)$$

The determination of surface modes is possible using the equation:

$$E - g\mu_B H_0 - 2SJ - 4SJ \left(1 - \gamma(\vec{k}_{\parallel}) \right) - SJ \left(\lambda + \frac{1}{\lambda} \right) - Ds - \frac{D^2 S s}{E - g_e \mu_B H_0 - DS} = 0, \quad (16)$$

which results from the combination of equations (9), (10) and (11). Numerical examples for spin waves are shown in Figures 1(a) and 1(b) for the low-frequency and high-frequency excitations, respectively.

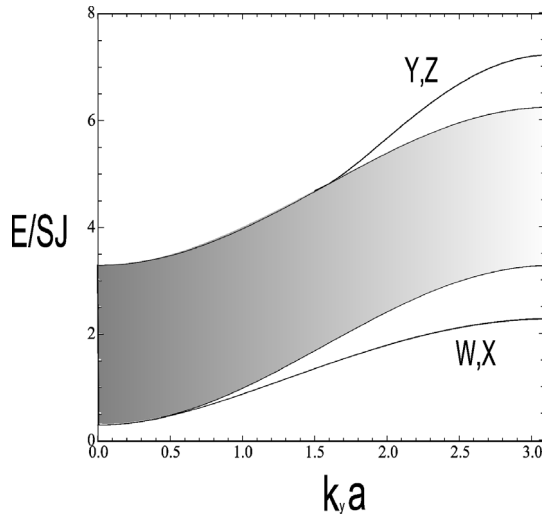


Figure 1a

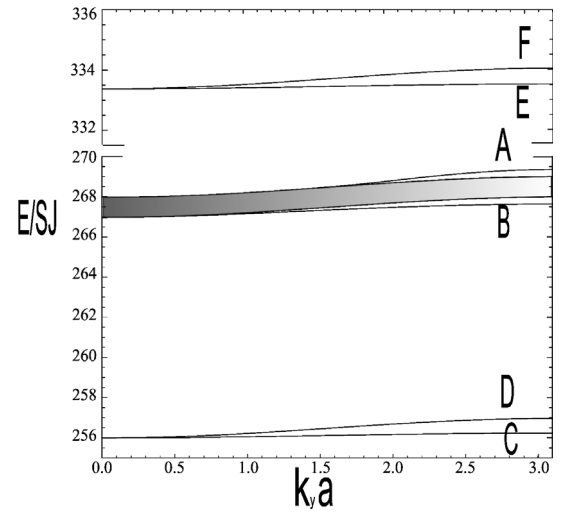


Figure 1b

Figure 1. Spectrum of spin-wave modes (in units SJ/\hbar) versus $k_y a$ for a semi-infinite narrow-band semiconductor (with $t = 0$) in the low frequency region (a) and high-frequency region (b). The parameter values are $\frac{D}{J} = 200$, $S = \frac{3}{2}$, $s = \frac{1}{2}$, $\frac{g\mu_B H_0}{SJ} = 0.3$, and $g_e = g$. The bulk spin-wave region is shaded, and the labelling of the surface spin-wave branches corresponds to:

Fig 1a W $\frac{I_s}{T} = 0.5$, $\frac{D_s}{D} = 1$; X $\frac{I_s}{T} = 0.5$, $\frac{D_s}{D} = 0.2$; Y $\frac{I_s}{T} = 2$, $\frac{D_s}{D} = 1$; Z $\frac{I_s}{T} = 2$, $\frac{D_s}{D} = 0.2$;

Fig 1b B $\frac{I_s}{T} = 0.5$, $\frac{D_s}{D} = 1$; A $\frac{I_s}{T} = 2$, $\frac{D_s}{D} = 1$; C $\frac{I_s}{T} = 0.5$, $\frac{D_s}{D} = 0.98$; D $\frac{I_s}{T} = 2$, $\frac{D_s}{D} = 0.98$;
E $\frac{I_s}{T} = 0.5$, $\frac{D_s}{D} = 1.02$; F $\frac{I_s}{T} = 2$, $\frac{D_s}{D} = 1.02$.

The choice of parameters is the same as in the work [9], taken as approximate values appropriate to the $S = \frac{3}{2}$ ferromagnet CdCr₂Se₄, which is usually considered to be a narrow-band material. Qualitatively, our results are the same as of Goplan and Cottam, meaning that surface spin waves appear as “acoustic” and “optical”, depending on the ratios $\frac{I_s}{T}$ and $\frac{D_s}{D}$. We confirm the result of [9] that in the case of low-frequency excitations, the surface spin-wave frequencies depend strongly on $\frac{I_s}{T}$, but only weakly on $\frac{D_s}{D}$. In the

case of high-frequency excitations the reverse applies (Fig. 1b), although there are some quantitative differences compared to [9].

More complicated case of the superlattice, where the motive consists of two planes at the surface and in the bulk ($N_0 = N = 2$) is also analyzed numerically. Results are shown in Figure 2 for a different set of parameters for low-frequency region. As expected, we have two bulk regions and we examined only the influence of the ratio $\frac{I^S}{T}$. We can conclude that surface spin waves appear as “acoustic” and “optical”, and they strongly depend on this ratio. We did not show results for high-frequency region, since in that case, for the superlattice where the motive consists of two planes at the surface and in the bulk, bulk regions degenerate into single lines.

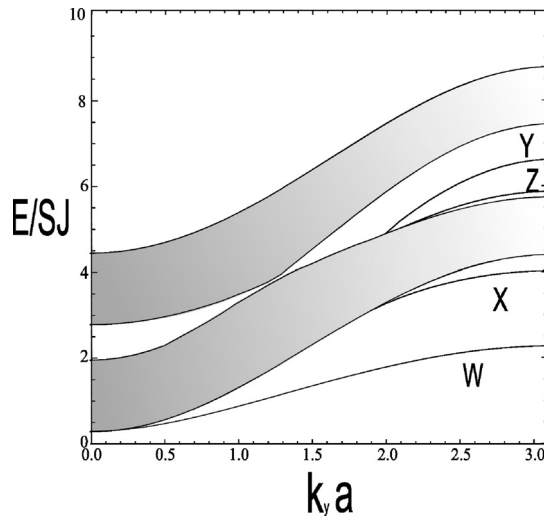


Figure 2. Dispersion curves of the spin-wave modes localized at the surface for $N_0 = N = 2$ in the low frequency region. The parameter values are $\frac{D_1}{J} = \frac{D_1^S}{J} = 200$, $\frac{D_2}{J} = \frac{D_2^S}{J} = 100$, $S_1 = S_1^S = \frac{3}{2}$, $S_2 = S_2^S = \frac{5}{2}$, $s = \frac{1}{2}$, $\frac{g\mu_B H_0}{SJ} = 0.3$, and $g_e = g$. The bulk spin-wave region is shaded, and the labelling of the surface spin-wave branches corresponds to W and X, $\frac{I^S}{T} = 0.5$, $\frac{I^S}{T} = 0.3$; Y and Z $\frac{I^S}{T} = 2$, $\frac{I^S}{T} = 1$.

3. Conclusion

The aim of this study was to analyze, theoretically, bulk and surface magnetic excitations of FMS’s superlattice using transfer matrix formalism, developed by Barnas [14] and generalized further by our team [13]. We considered the narrow-band limit, where the hopping exchange interaction of conduction electrons can be omitted. To our knowledge, there is no investigation on magnetic excitations of thin FMS’s films in the current literature. It would be of significant importance to expand our investigation onto these systems, which are the most interesting from the experimental point of view.

Acknowledgments

This work was supported by the Ministry of Science and Technological Development of the Republic of Serbia, Grant No. 141018.

References

- [1] T. Jungwirth, Jairo Sinova, J. Mašek, J. Kučera, A.H. MacDonald, *Rev. Mod. Phys.* **78**, 809 (2006).
- [2] I. Zutic, J. Fabian, S. Das Sarma, *Rev. Mod. Phys.* **76**, 323 (2004).
- [3] E.L. Nagaev, *Phys. Rep.* **346**, 387 (2001)
- [4] S.V. Vonsovski, J.A. Izyumov, *Usp. Fiz. Nauk* **1**, 4 (1962).
- [5] S.V. Vonsovski, J.A. Izyumov, *Usp. Fiz. Nauk* **3**, 379 (1962).
- [6] A. Babenco and M.G. Cottam, *Solid State Commun.* **22**, 651 (1977).
- [7] A. Mauger and D.L.Mills, *Phys. Rev. B* **28**, 6553 (1983).
- [8] J. M. Wesselinowa, *Phys. Status Solidi B* **120**, 585 (1983).
- [9] Sudha Gopalan and M.G. Cottam, *Phys. Rev. B* **42**, 10311 (1990).
- [10] J. M. Wesselinowa, E. Kroumova, N. Teofilov, W. Nolting, *Phys. Rev. B*, **57**, 6508 (1998).
- [11] J. M. Wesselinowa, P. Entel, *JMMM* **236**, 357 (2001).
- [12] A. Urbaniak-Kuncharczyk, *Phys. Status Solidi B* **186**, 263 (1994).
- [13] M. Pavkov, M. Škrinjar, D. Kapor, M. Pantić and S. Stojanović: *Int. J. Mod. Phys.B* **15**, 172369 (2001).
- [14] J. Barnas, *Phys. Rev. B* **45**, 10427 (1992)

Correction of the H_β Spectral Line Profile for the Influence of the Neighbour Hydrogen Lines

S. Djurović, I. Savić

*Faculty of Sciences, Department of Physics,
Trg Dositeja Obradovica 4, 21000 Novi Sad, Serbia*

Received: december 9, 2009

Abstract

The influence of the neighbour hydrogen lines H_α and H_γ on the H_β spectral line profile has been studied in the electron density range of $(2 - 7) \cdot 10^{23} \text{ m}^{-3}$. Except for the well defined line maxima and continuum level, this influence also can be important for the procedure of the electron density determination by using halfwidth of the H_β profile. It is especially important for the electron densities above $6 \cdot 10^{23} \text{ m}^{-3}$. For the analysis of the mentioned influence, theoretical profiles were used and the results were applied for the correction of experimental H_β profiles. The analysis showed that the intensity of the blue H_β wing can be higher by up to 35%, which leads to an error of 7% in the electron density determination for the highest electron density considered.

Key words: Plasma, Stark broadening, H_β spectral line

1. Introduction

The knowledge of theoretical and experimental profiles of hydrogen Balmer H_β line is very important for plasma diagnostics purposes. The method for the determination of electron density using the Stark broadened profiles of Balmer beta line is a standard technique in plasma spectroscopy. However, it should be noted that the accuracy of the density diagnostics from the measurement of the line halfwidth is in fact limited by the existence of the characteristic peaks of H_β profile and due to the continuum level determination problem. This is the reason why other methods for density determination have been proposed [1-4]. These methods are based, for example, on fitting exclusively the experimental line wings [1,2] or areas under maxima [2,5] to VCS profiles [6]. It was shown in [34] that methods using the whole experimental profiles for the χ^2 -minimization fitting provide density values that are by about 10% lower than those determined from the halfwidth. Contrary, fitting only the parts of experimental profiles could lead to higher electron densities [3,4] than the real ones. The inconsistency of the fitting output might be a result of insufficiently refined theoretical models [6,7] and profiles that lack to reproduce the real interrelations of various physical effects. For example, in the case of VCS profiles, which in the range of low density exhibit three times larger dip than in the experiment, this leads to the fitting output of lower electron densities [3]. Here we should point out that the fitting program [1]

shows 2 – 3 times lower electron densities than the ones obtained from H_β halfwidths, which was not observed by the comparison of the whole profiles by any other author [3]. Comments of this and other fitting methods [1,2,8-10] are given in [11]. Furthermore, theoretical H_β profiles [6,7] are symmetrical while experimental ones show both peak and body asymmetry. This is the reason why the fitting procedures used in the past often avoided the central region of the line [3,4]. Even if there exist the differences between theoretical and experimental profiles [6,7], for the electron densities above 10^{22} m^{-3} the line halfwidth is highly sensitive to the Stark broadening. Hence, the halfwidth method is rather reliable for the determination of electron density with a relative error of only about 6% [12]. This is true only if experimental profiles are well defined. Very often it is not the case, and the problem with peak intensity and continuum level determination arise. This could be minimized by using appropriate theoretical profiles.

New theoretical models based on the effects of microfield nonuniformity and electron impact shifts [13] and the standard theory and computer simulations with separately included quadrupolar and quadratic Stark effects [14], finally made it possible fitting of the whole asymmetric experimental H_β profile. This is especially important for the electron densities higher than 10^{23} m^{-3} . Possibilities of fitting the whole H_β profile, for electron densities lower than 10^{23} m^{-3} using symmetrical theoretical profiles [6,7,15,16] are described in [17]. Even with this, one more problem still exists. The problem is the influence of the neighbour hydrogen lines, especially of the H_γ on the H_β spectral line profile. In both techniques, using halfwidth measurements and fitting of the whole profile, especially for higher electron densities where hydrogen lines are very broad, this effect can increase the error of the electron density determination.

The aim of this work is to analyze the influence of the overlapping of the neighbour hydrogen lines on the H_β spectral line. Experimental profiles are obtained from T-tube plasma, with electron densities in the range of $(2-7) \cdot 10^{23} \text{ m}^{-3}$ and electron temperatures between 19 and 34 kK.

2. Experimental Setup and Plasma Diagnostics

The plasma was produced from an electromagnetically driven T-tube, having a diameter of 27 mm and being supplied with a reflector. The T-tube was energized using a $4 \mu\text{F}$ capacitor bank, charged up to 20 kV. The filling gas was hydrogen at a pressure of 300 Pa. Spectroscopic observations of plasma were performed using a 1 m monochromator and a photomultiplier. The observation point was fixed at 4 mm in front of the reflector. Photomultiplier signals were recorded on an oscilloscope. The H_β profiles were scanned at close intervals using successive discharges over the wavelength range of $\pm 30 \text{ nm}$ from the line centre. More details on this experiment can be found in Refs. 13 and 14.

Electron densities of the T-tube plasma, ranging from $2.28 \cdot 10^{23} \text{ m}^{-3}$ to $7.30 \cdot 10^{23} \text{ m}^{-3}$, were determined from Stark widths of the H_β line profiles. These measurements were performed in conjunction with theoretical calculations by Griem [7]. The estimated uncertainties of the electron densities did not exceed $\pm 9\%$. Electron temperatures, ranging from 19400 K to 34000 K, were determined from the line-to-line continuum ratios for the H_β line [18]. The uncertainties of electron temperature measurements were between $\pm 8\%$ and $\pm 15\%$, for the lower and higher values respectively.

3. Analysis of the Influence of the Neighbour Hydrogen Lines on the H_β Profile

In this analysis, three first lines, viz., H_α , H_β and H_γ , in the hydrogen Balmer series are considered. The illustration of the positions of these lines on the wavelength scale is shown in Figure 1.

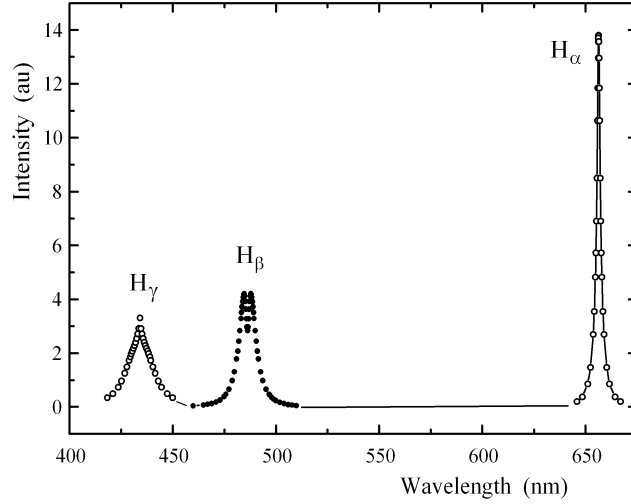


Figure 1. Illustration of the H_α , H_β and H_γ positions.

The same figures also show the H_α and H_γ intensities in the H_β profile region.

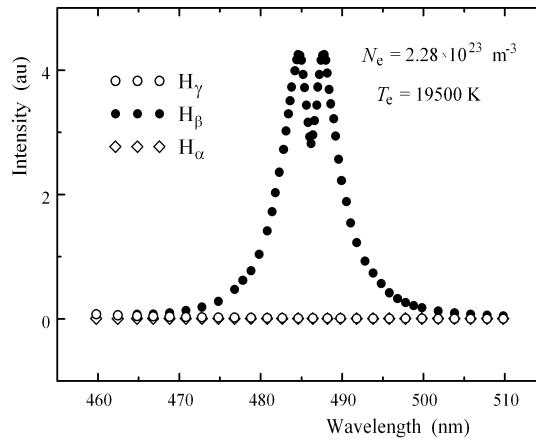


Figure 2. Theoretical H_β line profile [7] with corresponding H_α and H_γ theoretical intensities for electron density of $2.28 \cdot 10^{23} \text{ m}^{-3}$.

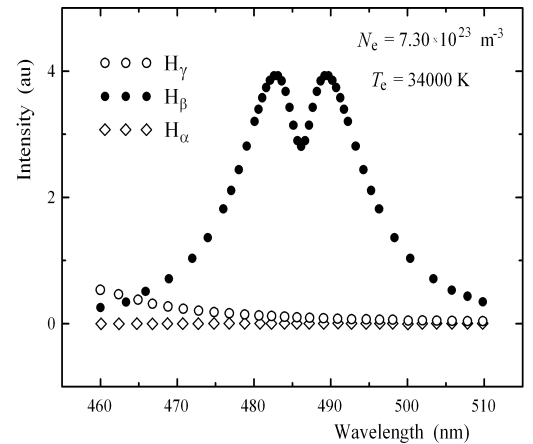


Figure 3. Theoretical H_β line profile [7] with corresponding H_α and H_γ theoretical intensities for electron density of $7.30 \cdot 10^{23} \text{ m}^{-3}$.

These influences are calculated for the different positions along the H_β profile, namely, in the centre of the line λ_0 , at the line maxima $\Delta\lambda_{\max}$, at the distance $\Delta\lambda_{1/2}/2$ and $\Delta\lambda_{1/2}$ from the line centre in both directions (left and right from the line centre). The $\Delta\lambda_{1/2}$

For this illustration, the theoretical profiles [7] of the lines are used. The H_α line is far from the H_β line profile, and in most cases the influence of H_α can be negligible, while H_γ is relatively close, and its influence should be considered.

Theoretical H profiles [7] were generated for our experimental conditions, electron densities ($2.28, 2.73, 3.30, 4.09, 5.69$ and 7.30) $\cdot 10^{23} \text{ m}^{-3}$ and electron temperatures ($19400, 20200, 21200, 24200, 28000$ and 34000) K. The H_β profiles [7], which correspond to lower and higher experimental electron densities, are shown in Figures 2 and 3.

denotes the halfwidth of the H_β line profile. The positions for calculations of the influence are shown in Figure 4. The $I(H_\beta)$ intensities at the different positions along the H_β profile are shown in Table 1, together with the $I(H_\alpha)$, and $I(H_\gamma)$ intensities [7] for comparison.

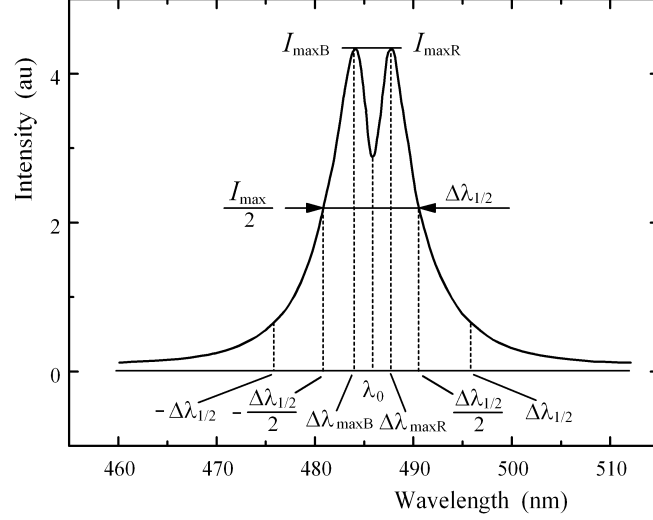


Figure 4. Illustration of the positions along the H_β profile at which calculations of the H_α and H_γ influences were performed.

Table 1. The $I(H_\beta)$ intensities at the different positions along the H_β profile and $I(H_\alpha)$, and $I(H_\gamma)$ intensities [7] at the same positions.

N_e ($10^{23}m^{-3}$)	T_e (K)	line	Intensities (a. u.)						
			$-\Delta\lambda_{\frac{1}{2}}$	$-\frac{\Delta\lambda_{\frac{1}{2}}}{2}$	$-\Delta\lambda_{\max B}$	λ_0	$\Delta\lambda_{\max R}$	$\frac{\Delta\lambda_{\frac{1}{2}}}{2}$	$\Delta\lambda_{\frac{1}{2}}$
2.28	19400	H_γ	0.0200	0.0161	0.0138	0.0129	0.0121	0.0107	0.0089
		H_β	0.6200	2.0600	4.2400	2.8200	4.2400	2.0600	0.6200
		H_α	0.0001	0.0001	0.0001	0.0001	0.0001	0.0001	0.0001
2.73	20200	H_γ	0.0288	0.0225	0.0190	0.0177	0.0163	0.0142	0.0116
		H_β	0.5800	2.0868	4.2073	2.8449	4.2073	2.0868	0.5800
		H_α	0.0001	0.0002	0.0002	0.0002	0.0002	0.0002	0.0002
3.30	21200	H_γ	0.0420	0.0318	0.0264	0.0242	0.0227	0.0190	0.0150
		H_β	0.6000	2.0804	4.1858	2.8761	4.1580	2.0804	0.6000
		H_α	0.0002	0.0003	0.0003	0.0003	0.0003	0.0003	0.0003
4.09	24200	H_γ	0.0690	0.0480	0.0385	0.0349	0.0318	0.0260	0.0203
		H_β	0.6100	2.0731	4.1622	2.9109	4.1622	2.0731	0.6100
		H_α	0.0003	0.0004	0.0004	0.0004	0.0004	0.0004	0.0005
5.69	28000	H_γ	0.1600	0.0960	0.0746	0.0643	0.0557	0.0443	0.0320
		H_β	0.5900	2.1140	3.9753	2.7746	3.9753	2.1140	0.5900
		H_α	0.0005	0.0006	0.0007	0.0007	0.0007	0.0008	0.0009
7.30	34000	H_γ	0.3100	0.1800	0.1146	0.0987	0.0856	0.0647	0.0450
		H_β	0.6000	2.0000	3.9286	2.8099	3.9286	2.0000	0.6000
		H_α	0.0009	0.0009	0.0010	0.0011	0.0011	0.0012	0.0014

It is obvious that the H_α intensities are very small in comparison with both the $I(H_\beta)$ and $I(H_\gamma)$ intensities and the influence of H_α on the H_β profile can be neglected in all considered cases. However, the influence of the H_γ on the H_β profile must be taken into account.

To investigate the influence of the neighbour lines on the H_β profile, total intensities $I(H_\gamma) + I(H_\beta) + I(H_\alpha)$, even if $I(H_\alpha)$ was negligible, were calculated at each of the above mentioned positions, and then the percentage intensities for which H_β line profile was raised were also calculated. The calculated corrections for different electron densities are given in Table 2.

Table 2. Percentages of the necessary correction of the H_β profile intensity at different positions.

N_e ($10^{23}m^{-3}$)	T_e (K)	Corrections (%)						
		$-\Delta\lambda_{\frac{1}{2}}$	$-\frac{\Delta\lambda_{\frac{1}{2}}}{2}$	$-\Delta\lambda_{\max B}$	λ_0	$\Delta\lambda_{\max R}$	$\frac{\Delta\lambda_{\frac{1}{2}}}{2}$	$\Delta\lambda_{\frac{1}{2}}$
2.28	19400	3.140	0.780	0.327	0.459	0.287	0.522	1.431
2.73	20200	4.746	1.076	0.454	0.625	0.391	0.685	1.994
3.30	21200	6.571	1.520	0.634	0.845	0.550	0.919	2.487
4.09	24200	10.202	2.281	0.926	1.198	0.768	1.257	3.297
5.69	28000	21.386	4.370	1.859	2.289	1.399	2.089	5.282
7.30	34000	34.131	8.295	2.858	3.430	2.159	3.190	7.178

The same results are graphically shown in Figure 5. The presented results show for which percentages the H_β line intensities should be reduced because of the influences of the H_α and H_γ .

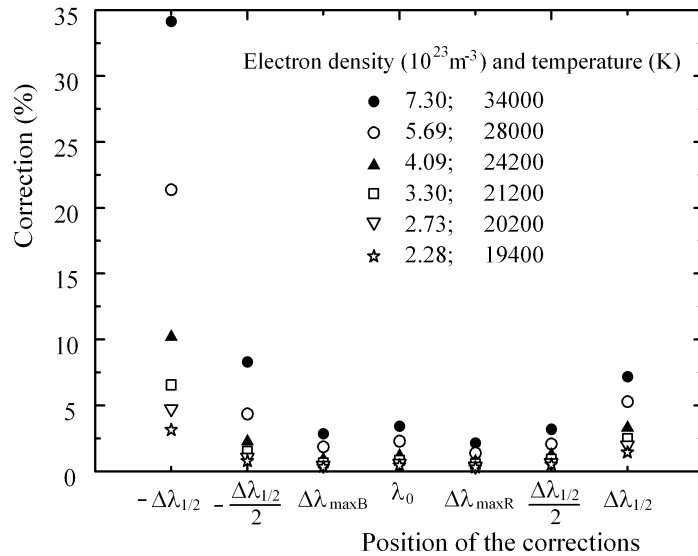


Figure 5. The calculated corrections of the H_β profile intensity at different positions.

4. Correction of the experimental profiles

Before the comparison of the pure experimental and corrected experimental profiles, the continuum was eliminated. For this purpose, the linear dependence of the continuum of the wavelength was assumed. The experimental H_β line profile correction is illustrated in Figure 6 for an electron density of $3.30 \cdot 10^{23} \text{ m}^{-3}$ and in Figure 7 for electron density of $7.30 \cdot 10^{23} \text{ m}^{-3}$.

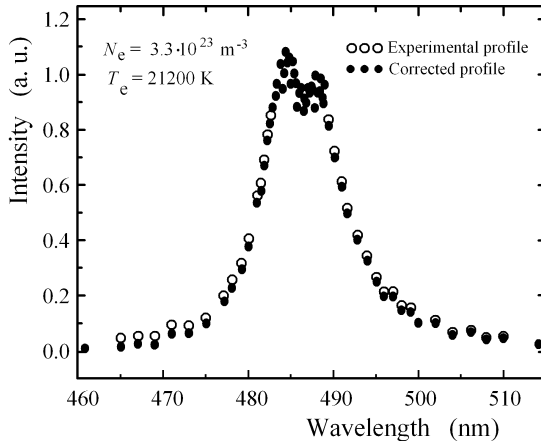


Figure 6. The H_β profile correction ($N_e = 3.30 \cdot 10^{23} \text{ m}^{-3}$).

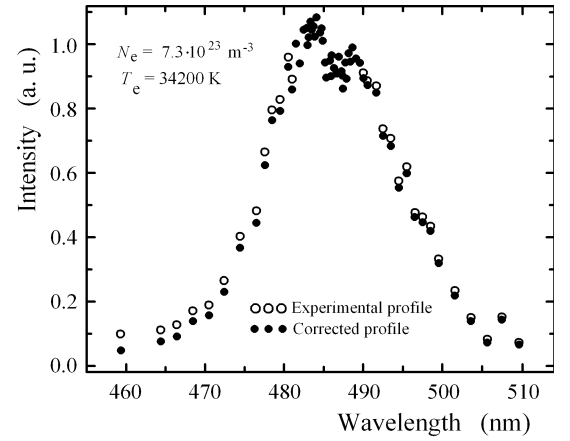


Figure 7. The H_β profile correction ($N_e = 7.30 \cdot 10^{23} \text{ m}^{-3}$).

Here, it should be pointed out that every experimental point in Figures 6 and 7 represent an average value of 6 independent measurements. It is obvious that experimental profiles are asymmetrical. The asymmetry of the whole profile is elaborated in Ref. [13] and asymmetry of the line maxima in Ref. [14]. Even though the experimental profiles are to a certain degree asymmetrical, for the analysis of the H_α , and H_γ influences, symmetrical theoretical profiles [7], (available at this moment) were used. In the region of the maxima of the experimental H_β profiles, only corrected points are presented because of overlapping of many points in a small area.

Table 3. Percentage of halfwidth and electron density correction after the H_β profile correction.

N_e (10^{23} m^{-3})	Corrections (%)	
	$\Delta(\Delta\lambda_{\frac{1}{2}})$	$\Delta(N_e)$
2.28	1.9	3.0
2.73	2.2	3.4
3.30	2.5	4.0
4.09	3.0	4.7
5.69	4.0	6.1
7.30	5.0	7.5

by the influence of the neighbour lines on the H_β profile is the same as the error

The values of electron densities given in the figures and tables of Paragraph 3 were obtained before the H_β profiles corrections. The H_β profile correction influences, of course, the halfwidth profile determination, and thus, the electron density determination. The percentage of the halfwidths and electron density reductions are given in Table 3. It is obvious that for electron densities above $6 \cdot 10^{23} \text{ m}^{-3}$ the error caused

of the electron density determination, which was estimated to be 6% [12]. Of course, it is assumed that the experimental profile is well defined, without large spread of the experimental points.

6. Conclusion

In this paper we analyzed the influence of the neighbour hydrogen lines overlapping on the H_β spectral line. The analysis was performed for the electron densities between $2.28 \cdot 10^{23} \text{ m}^{-3}$ and $7.30 \cdot 10^{23} \text{ m}^{-3}$, for which experimental work was performed. Based on the analysis, corrections were made of line intensities, halfwidths, and finally, of electron densities. The conclusion is that this type of correction must be performed for the electron densities above $6 \cdot 10^{23} \text{ m}^{-3}$.

This type of the H_β profile correction is one of the three critical elements for the determination of electron density if halfwidth of the H_β line is used. Other two elements are the determinations of maxima and continuum level. These two levels determine the level at which halfwidth of the line is to be measured. All three types of the experimental H_β line profile correction allow us to fit theoretical profiles to the whole experimental profile and use it for the electron density determination instead of the measurement of the halfwidth only.

In this work we used symmetrical theoretical H_β profiles [7] which are quite good for this type of analysis. For the fitting of the whole profile one should use asymmetrical theoretical profiles [13,14], which can better describe the shape of the experimental profile.

Acknowledgments

This work was supported by the Ministry of Science and Technological Development of the Republic of Serbia, under Project No. 141024.

References

- [1] S. R. Goode and J. P. Deavor, *Spectrochim. Acta, Part B* **39**, 813 (1984).
- [2] S.-K. Chan and A. Montaser, *Spectrochim. Acta, Part B* **44**, 175 (1989).
- [3] C. Thonmsen and V. Helbig, *Spectrochim. Acta, Part B* **46**, 1215 (1991).
- [4] I. Ishii, R. H. Clifford, A. Montaser, B. A. Palmer, and L. R. Lyman, Contributed paper of 17th FACSS Meeting Cleveland, OH, USA, (1990).
- [5] A. Montaser and S.-K. Chan, SCAN, CONVERT and NE: New computer programs for the determination of electron number density via Stark broadening, U. S. Copyright, Department of Chemistry, The George Washington University, Washington, DC, 20052, USA, (1989).
- [6] C. R. Vidal, J. Cooper, and E. W. Smith, *Astrophys. J., Suppl.* **25**, 37 (1973).
- [7] H. R. Griem, *Spectral Line Broadening by Plasmas*, Academic, New York, (1974).

-
- [8] M. Kuraica, N. Konjević, M. Platiša and D. Pantelić, *Spectrochim. Acta, Part B* **47**, 1173 (1992).
- [9] H. Zhang, C. Hsieh, I. Izshi, Z. Zeng, A. Montaser, *Spectrochim. Acta, Part B* **49**, 817 (1994).
- [10] T. K. Starn, N. N. Sesi, J. A. Horner, G. M. Hieftje, *Spectrochim. Acta, Part B* **50**, 1147 (1995).
- [11] M. Ivković and N. Konjević, *J. Res. Phys.* **28**, 239 (1999).
- [12] W. L. Wiese, D. E. Kelleher and D.R. Paquette, *Phys. Rev. A* **6**, 1132 (1972).
- [13] S. Djurović, D. Nikolić, I. Savić, S. Sörge and A. V. Demura, *Phys. Rev. E* **71**, 036407 (2005).
- [14] S. Djurović, M. Ćirišan, A. V. Demura, G. V. Demchenko, D. Nikolić, M. A. Gigosos, and M. . González, *Phys. Rev. E* **79**, 046402 (2009).
- [15] C. Stehlé, R. Hutcheon, *Astron. Astrophys. Suppl. Ser.* **140**, 93 (1999).
- [16] M. A. Gigosos and V. Cardenoso, *J. Phys. B: At. Mol. Opt. Phys.* **29**, 4795 (1996).
- [17] R. Žikić, M. A. Gigosos, M. Ivković, M. Á. González and N. Konjević, *Spectrochim. Acta, Part B* **57**, 987 (2002).
- [18] H. R. Griem, *Plasma Spectroscopy*, McGraw-Hill, New York (1964).

Phase Transition Temperature Shifts in Binary Cholesteric Liquid Crystalline Mixtures Doped with some Chiral Nonmesogenic Additives

D.Ž. Obadović¹, M. Stojanović¹, S. Jovanović-Šanta², J. Nikolov¹, D. Lazar¹,
M. Cvetinov¹, A. Vajda³ and N. Éber³

¹*Department of Physics, Faculty of Sciences, University of Novi Sad,
Trg D. Obradovića 4, 21000 Novi Sad, Serbia*

²*Department of Chemistry, Faculty of Sciences, University of Novi Sad,
Trg D. Obradovića 3, Novi Sad, Serbia*

³*Research Institute for Solid State Physics and Optics of the Hungarian Academy of
Sciences, H1525 Budapest, P. O. Box 49, Hungary*

Received: December 11, 2009

Abstract

We have investigated the influence of three chiral nonmesogenic estradiol derivatives on the physical characteristics of the binary mixture of cholesteric liquid crystals cholesteryl myristate and cholesteryl enantate. We observed that the addition of the chiral additives induces a shift of the phase transition temperatures. The characterization of the mesophases has been made by X-ray diffraction. These data enabled the determination of some structural parameters of the mixtures: the thickness of smectic layers and the average distance between the long axes of neighbouring molecules.

Key words: X-ray diffraction, estradiol derivatives, cholesteric liquid crystals

1. Introduction

This work represents the continuation of our studies on binary and multicomponent mixtures of cholesteric liquid crystals, undertaken with the aim to obtain systems with stable mesophases and transition temperatures close to room temperature [1,2]. Estradiol derivatives have a steroidal configuration similar to that of the cholesteryl backbone, which makes them suitable as chiral additives in cholesteric mixtures even though they do not have mesophases. In natural biological systems, estradiol and estradiol derivatives play a significant physiological role [3].

In the present paper we investigate the influence of some estradiol derivatives on the mesophase behaviour of a binary mixture of cholesteryl laurate and cholesteryl enantate. Measurements have been carried out to identify the types and textures of mesophases and determine the phase transition temperatures by optical microscopy. X-ray measurements have also been performed to confirm the structure of mesophases and determine structural parameters.

2. Experimental

2.1. Methods and equipments

The optical studies were performed using a polarizing microscope (Carl Zeiss, Jena) in transparent light using crossed polarizers. A hot stage allowed controlled heating and cooling of the sample. Homeotropical alignment of the liquid crystal was obtained by evaporation of gold onto the glass plate using the vacuum evaporator JEOL JEE-4B.

Unoriented samples were investigated by X-ray diffraction in the transmission geometry on a conventional powder diffractometer (Seifert V-14) equipped with an automatic high temperature kit Paar HTK-10, using $\text{CuK}\alpha$ radiation at 0.154 nm. The X-ray diffraction data allowed the determination of structural parameters characteristic for the molecules and the mesophase they form [4]. Namely, the layer spacing (d) in the smectic A* (SmA^*) phase and the average intermolecular distance (D) (i.e. the mean distance between the long axes of the neighbouring parallel molecules) could be obtained using Bragg's law: $\lambda = 2x \sin \theta$. Here, the distances $x = (d \text{ and } D)$ were calculated from the positions of the small angle and the large angle diffraction peaks, respectively.

2.2. The chiral additives

The investigated chiral additives, 17 β -estradiol 3-benzylether 17-acetate (**1**), 17 β -estradiol diacetate (**2**) and 17 β -estradiol dipropionate (**3**), are well known compounds [5]. We synthesized them, however, by modified methods. Compound **1** was synthesized by benzylation of estradiol in dry mixture of methanol and acetone in the presence of potassium carbonate, followed by acetylation of the resulting benzyl ether of estradiol by acetic anhydride in dry pyridine. Compounds **2** and **3** were synthesized from estradiol, by the reactions of esterification with acetic anhydride and propionic anhydride in dry pyridine, respectively. The chemical formulae of the prepared chiral additives are given in Figure 1. Compounds **1** to **3** are non-mesogenic, their melting points are listed in Table 1.

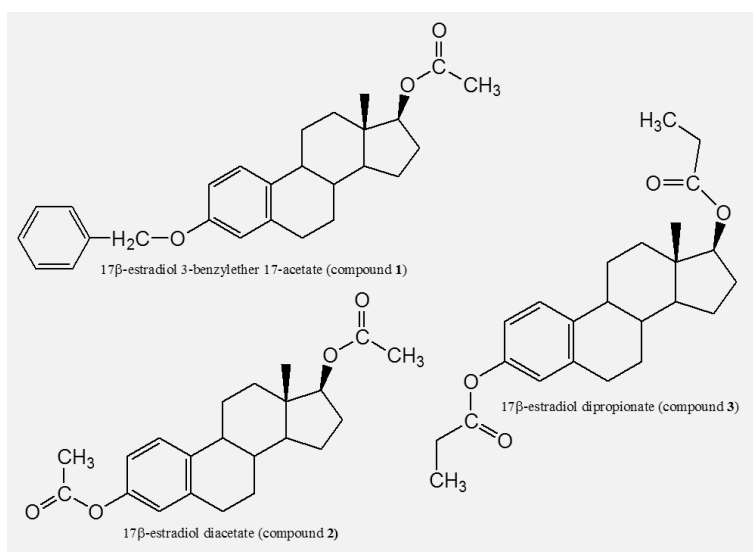


Figure 1. Chemical structures of the chiral additives **1**, **2** and **3**

Table 1. The phase sequences and phase transition temperatures of the pure compounds.

Compound	Phases and transition temperatures (°C)
Cholesteryl myristate	I 84.6 Ch 79.1 SmA* 71 Cr
Cholesteryl enantate	I 114 Ch 99.5 Sm A* 92.5 Cr
1	Cr 101-107 I
2	Cr 121-124 I
3	Cr 101-104.5 I

2.3. The mixtures

In order to investigate the influence of the synthesized chiral additives on the mesophase behaviour we had to prepare first a binary mixture, **Mixbin**, which contained cholesteryl myristate and cholesteryl enantate in the 1 : 1 ratio by weight. **Mixbin** served as a reference mixture for our studies. Before preparing the reference mixture, its components have been checked by polarizing microscopy. The obtained phase sequences and phase transition temperatures are also listed in Table 1, and they show a good agreement with the existing literature data [6].

The chiral additives were tested in three-component mixtures (**Mix1**, **Mix2** and **Mix3**), composed of **Mixbin** (90% by weight) and one of the chiral derivatives (10% by weight of **1**, **2** and **3**, respectively).

3. Results and discussion

Optical microscopic studies have been carried out on the reference mixture **Mixbin**, as well as on the three-component mixtures **Mix1** to **Mix3**. Observation of the textures allowed to determine the phase sequences and the phase transition temperatures. Results of the observations are summarized in Table 2. The layer structure in the SmC phase of compound **II** is characterized by one reflection at a small angle $2\theta = 3.1^\circ$. In mixtures **Mix1** and **Mix2**, similarly, one reflection peak could be found at small angles at the same position as for the rod-like molecule, indicating the presence of the SmC phase.

In all investigated mixtures, focal conic polygonal textures were observed. This texture is characteristic to such cholesteric liquid crystals where the cholesteric quasi-layers have an oblique orientation with respect to the substrates, i.e., the helical axis is strongly tilted. Such an orientation occurs if the surface area is occupied by the polygonal base of a focal conic domain. However, formation of such a domain, although it reduces the surface energy, is also accompanied by an increase of the “bulk” energy due to the director distortions. The energy balance dictates that the focal conic domains has to be larger than some critical size in order to become stable [7-10].

Figure 2a presents an example for this texture of the cholesteric (Ch) phase observed in a homeotropic cell. The observed colour is due to the selective reflection originating from a helical structure of the short pitch.

The focal conic texture of the SmA* phase in a homeotropic cell are shown in Figure 2b. The apparent optic axis is parallel to the layer normal direction in the SmA* phase. In many SmA* materials, the layer normal direction points to the centre of the focal conic, i.e. the layers orient tangentially in a circular focal conic domain.

Table 2. Phase transition temperatures, width of the phase temperature ranges and the shift of the phase transition temperatures in the investigated mixtures. All temperatures are given in °C.

		Mixture			
		Mixbin	Mix1	Mix2	Mix3
Transition temperature	I → Ch	67.6	65.6	54.1	62.4
Transition temperature	Ch → SmA*	65.0	57.0	44.1	57.0
Transition temperature	SmA* → Cr	55.0	43.7	38.0	41.0
Phase temperature range	Ch	2.6	8.6	10.0	5.4
Phase temperature range	SmA*	10.0	9.3	6.1	16.0
Temperature shift	I → Ch		2.0	13.5	5.2
Temperature shift	Ch → SmA*		8.0	20.9	8.0
Temperature shift	SmA* → Cr		7.3	17.0	14.0



Figure 2a

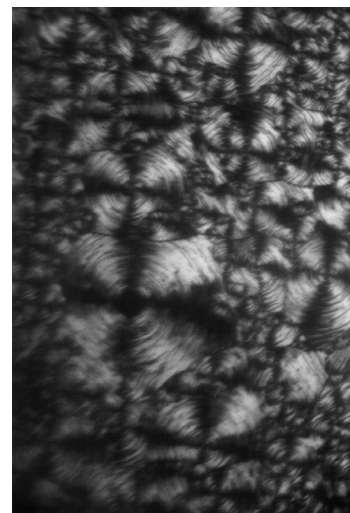


Figure 2b

Figure 2. Textures of **Mixbin**: a) Focal conic polygonal texture observed in the Ch phase.
b) Texture with circular focal conic domains in the SmA* phase.

The optical observations have shown that the phase sequence of the mixtures (Table 2) is not affected by the chiral additives: in all mixtures a sequence of isotropic (I) - cholesteric (Ch) - smectic A* (SmA*) - crystal (Cr) was found. The phase transition temperatures are, however, shifted toward lower values in the three-component mixtures **Mix1** to **Mix3** com-

pared to the binary mixture **Mixbin**. The largest temperature shifts have been recorded after the addition of the chiral non-mesogenic additive **2**. The phase transition temperatures did not shift uniformly, hence the width of the temperature range of the mesophases is also affected by the additives. Interestingly, all three additives induced a broadening of the Ch phase range, compound **2** being the most effective (**Mix2** exhibited a 10 °C wide cholesteric phase. The widest SmA* phase (~ 16 °C) was registered in the case of **Mix3** (Table 2).

Having determined the phase sequences by microscopy we also performed X-ray diffraction studies on unoriented samples of the binary (**Mixbin**), as well as of the three-component (**Mix1** to **Mix3**) mixtures, in all phases they exhibited. The relevant structural parameters obtained from the X-ray diffraction data are listed in Table 3. As examples, diffraction profiles of unoriented samples of **Mixbin** and of one ternary mixture (**Mix3**) are depicted in Figure 3 for different temperatures.

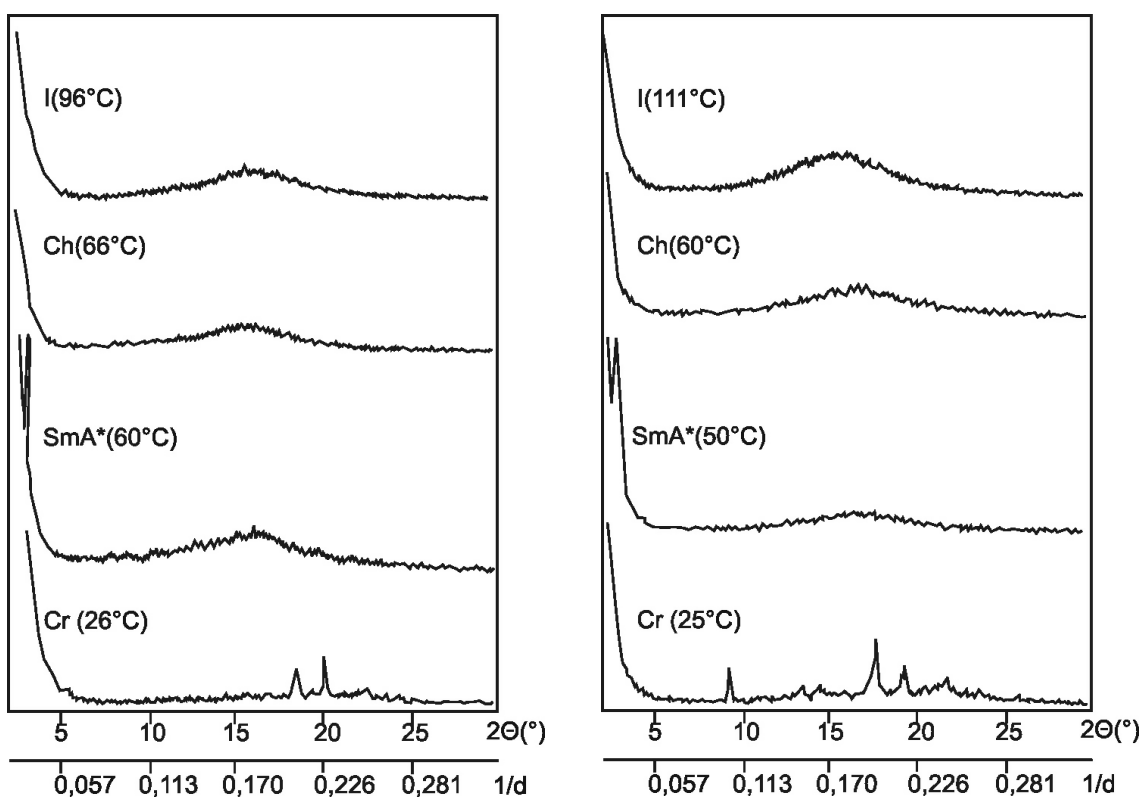


Figure 3a

Figure 3b

Figure 3. X-ray diffraction profiles for: a) **Mixbin** and b) **Mix3**

The analysis of X-ray diffraction profile of the SmA* phase showed the presence of a strong reflection at small angles, indicating the presence of a layer structure with layer spacing d ; the diffuse broad peak appearing in the 2θ range of $10 - 25^\circ$, with a maximum at 16.5° corresponding to the average intermolecular distance (D).

One can notice in Table 3 that the chiral additive **3** induces an increase in the smectic layers thickness in the SmA* phase compared to that of **Mixbin**. It is probably due to the

steric influence of bulky substituents at positions 3 and 17 of the backbone of the chiral additive **3**, which in the ternary mixture **Mix3** alters the packing of the host molecules of **Mixbin**.

Table 3. Structural parameters of investigated mixtures for all observed phases at temperature T [°C]: angles corresponding to the reflection peaks 2θ [°], smectic layer thickness d [Å] (error of measurements δ_d was about ± 0.1 Å), average intermolecular distance D [Å] (error of measurements δ_d was about ± 0.03 Å).

Mixture	T [°C]	2θ [°]	d [Å]	D [Å]
Mixbin	96 (I)	16.0		5.53
	66 (Ch)	16.4		5.4
	60 (SmA*)	2.9	30.4	5.37
Mix1	111 (I)	16.0		5.53
	63.5 (Ch)	16.4		5.4
	51 (SmA*)	3.5	25.2	5.33
Mix2	93 (I)	16.2		5.46
	50 (Ch)	16.8		5.27
	42 (SmA*)	3.5	25.2	5.21
Mix3	111 (I)	16.0		5.53
	60.4 (Ch)	16.9		5.24
	50 (SmA*)	2.7	32.7	5.18

On the other hand, the d values for **Mix1** and **Mix2** are by almost 15% smaller than in **Mixbin** (Table 3). It could be because the substituents in the positions 3 and 17 of the backbone of the estradiol derivatives **1** and **2** are less bulky, so they allow better packing of the host molecules in the ternary mixtures.

In the cholesteric and isotropic phases no small angle reflections are detectable, indicating the lack of positional order; only the broad peaks at larger angles are present (Figure 3) corresponding to the average intermolecular distance D . As can be seen from Table 3, the additives have practically no influence on D in the isotropic phase. However, some reduction of D can be seen in the Ch phase of the ternary mixtures, which becomes more pronounced in the SmA* mesophase. This indicates that a higher packing density of the molecules is favoured in the presence of the additives, than in the pure cholesteric binary mixture.

4. Conclusion

The results of the studies of the ternary mixtures of cholesteric liquid crystals with non-mesogenic chiral estradiol derivatives **1** - **3** have shown a significant shift of the mesomorphic phase transitions toward lower temperatures, compared to those of the reference mixture. From the X-ray diffraction data of unoriented samples we have determined the

average intermolecular distance, D , and the smectic layer spacing, d . It was shown that the smectic layer spacing in the SmA* phase of **Mix3** is bigger, while in **Mix1** and **Mix2** it is smaller than in the reference mixture. The reduction of the average intermolecular distances indicates a higher packing density of the molecules in the ternary mixtures than in the reference one.

Acknowledgments

This work was supported by research Grant No. 141020 and No. 142052B from the Ministry of Science and Technological Development of the Republic of Serbia, the Hungarian National Science Funds OTKA K61075, the ESF-COST D35 WG-13/05, and the SASA-HAS bilateral exchange project.

References

- [1] D.Ž. Obadović, A. Vajda, T. Tóth-Katona and R. Marinković-Nedućin, *Mol.Cryst.Liq.Cryst.* **265**, 135-142 (1995).
- [2] D.Ž. Obadović, A. Vajda, M. Stančić, S. Jovanović-Šanta, J. Petrović, D. Lazar, *Phase Transitions* **74**, 509-519 (2001).
- [3] J.C. Herve, F. Pluciennik, F. Verrecchia, B. Bastide, B. Delage, M. Joffre, J. Deleze, *J. Membrane Biol.* **149**, 179-187 (1996).
- [4] D.Ž. Obadović, M. Stojanović, S. Jovanović-Šanta, D. Lazar, A. Vajda and N. Éber, *International Journal of Modern Physics B* **20**, No.21, 2999-3013 (2006).
- [5] http://www.chemicalbook.com/ProductChemicalPropertiesCB2326852_EN.htm
- [6] G.W. Gray and P. A. Windsor, *Liquid Crystals and Plastic Crystals*, Vol. 2, J. Wiley and Sons, New York, 1974.
- [7] M. Yada, J. Yamamoto and H. Yokoyama, *Langmuir* **18**, 7436-7440 (2002).
- [8] Y. Bouligand, *J. Phys.* **33**, 715 (1972).
- [9] C.S. Rosenblatt, R. Pindak, N.A. Clark, R.B. Meyer, *J. Phys.*, **38**, 1105 (1977).
- [10] D. Demus, L. Richter, *Textures of Liquid Crystals*, Verlag Chemie: Weinheim, Germany, 1978.

Dielectric Properties of Molecular Inclusion Complex of β -cyclodextrin and iron fumarate

Nataša Lalović, Agneš Kapor, Željka Cvejić, Sonja Skuban, Srđan Rakić, Stevan Jankov
*Department of Physics, Faculty of Sciences, University of Novi Sad,
Trg Dositeja Obradovica 4, 21000 Novi Sad, Serbia*

Received: December 17, 2009

Abstract

Dielectric properties of β -cyclodextrin and Fe(II)-fumarate were studied in the form of inclusion complex (BCDFe) and basic compounds of β -cyclodextrin (BCD) as “host” molecule and Fe(II)-fumarate as a small molecule included as the “guest” into the molecule of β -cyclodextrin. Measurements were performed at several frequencies of 10, 10^2 , 10^3 , 10^4 and 10^5 Hz at the temperatures starting from room temperature 25°C up to the sample melting point, which is 220°C for the complex BCDFe and BCD and 160°C for Fe(II)-fumarate. Dielectric properties of these substances were studied with the objective to explain the processes occurring within the complex during the complexing and the changes in the complex itself.

Key words: β -cyclodextrin complex, Fe(II)-fumarate, dielectric properties, conductivity, comparative study

1. Introduction

Cyclodextrins are natural compounds with high possibilities of application in the pharmaceutical industry. They are macrocyclic oligosaccharides. The α -, β - and γ -cyclodextrins, consisting of 6, 7, and 8 glucopyranous units (Fig. 1.) are used most. They are characterized by the ring structure with cavities. When the number of glucopyranous units increases, so increases the ring diameter and the cavities within it [1].

The shape of cyclodextrin molecules reminds to flattened cone. They possess hydroxyl groups OH-2, OH-3 and OH-6. Secondary hydroxyl groups (OH-2 and OH-3) are on the broader, while the primary ones (OH-6) are on narrower side of the cylindrical molecule. There exists a strong hydrogen bond between the OH-2 and OH-3 groups, with the OH-3 group acting as proton donor. The ratio of the strengths of hydrogen bonds in cyclodextrins is the following: $\alpha\text{-CD} < \beta\text{-CD} < \gamma\text{-CD}$. The OH-6 groups can also be bonded by hydrogen bonds on the lower side of the molecule, but these bonds are destabilized by dipolar effects, decay easily in water, and usually do not appear in cyclodextrin crystals.

Cyclodextrin molecules bind hydroxyl groups at the outer sides of the cavities and inside the molecule they bind hydrogen atoms. In water solutions, these hydrophobic cavities contain 3 (α -CD), 7 (β -CD) or 9 (γ -CD) weakly bound water molecules. Their

density inside the cavities is small, and they are large enough to accept more molecules. This means that cyclodextrins can bind nonpolar aliphatic and aromatic molecules of the corresponding dimensions. They are bonded in the ratio 1:1, 2:1 and 1:2, depending on the nature of the guest molecule [2,3].

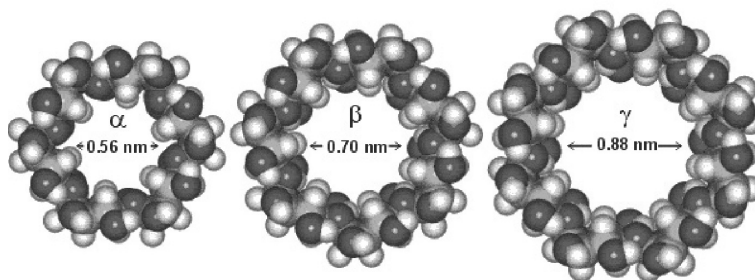


Figure 1. Structure of α -, β - and γ -cyclodextrin.

The study of crystalline β -cyclodextrin indicated that there are three modes of packing the molecules (Fig. 2.). Most important characteristics of the β -cyclodextrin are given in the Table 1.

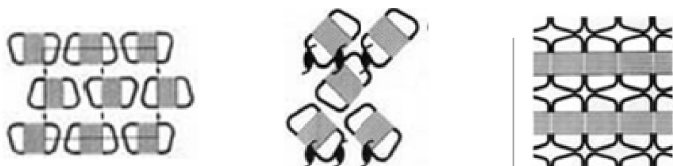


Figure 2. Possible ways of packing of β -cyclodextrin.
a) brick wall; b) herring bone; c) channel structure.

Table 1. Some characteristics of β -cyclodextrin.

Molecular formula	$C_{42}H_{70}O_{35}$
Relative molecular mass	1135
Diameter of internal cavity (Å)	7
Solubility in water (g/100 ml; 25 °C)	1.85
Melting point (°C)	255-265
Number of water molecules in the cavity	7

Fe(II)-fumarate (*ferrous fumarate* or *iron(II)-fumarate*) is the compound of fumaric acid and divalent iron representing fine red-brown powder, sparingly soluble in water (solubility 0.14 g/100 cm³, 25 °C) and alcohol. It is hard to melt, and stays stable even above 200 °C.

Fumaric acid is *trans*-1,2-ethylenedicarboxylic acid, rational formula $C_4H_4O_4$. There is a generally accepted formula in the literature presenting Fe(II)-fumarate in the manner shown at Fig. 3.

Fe(II)-fumarate is well known pharmacological agent. Its medical application is based on the following facts. It is assumed that about 20 – 30% of the world population suffers from hypsideremy (lack of iron and sideremyenic anemia), so that the prevention and therapy of such conditions are permanently existing problems in human medicine. In order to overcome this problem, a great number of pharmaceuticals based on ferrous or ferric iron are used. Oral therapy is based on medicaments containing salts of divalent iron such as ferrosulphate, ferrofumarate, ferrogluconate etc. with Fe(II)-fumarate most broadly used. This fact is due to its good properties such as good absorption in the organism and low toxicity. Good absorption in the organism originates from fumaric acid, which is an intermediate in the cycle of tricarboxylic acids and as such is abundant in living organisms (Crebbs cycle or lemon acid cycle) [4,5]. By complexing the Fe(II)-fumarate with β -cyclodextrin, the complex becomes soluble in water, making it superior to those of the non-complexed active materials (Fe(II)-fumarate) [6].

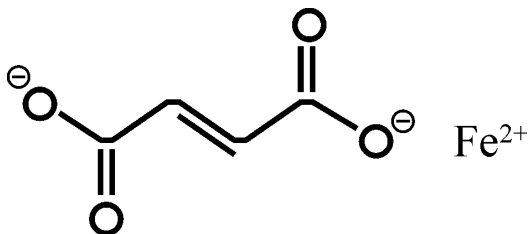


Figure 3. General formula of Fe(II)-fumarate.

2. Experiment

Measurement of electric properties of samples of inclusion complex, Fe(II)-fumarate and β -cyclodextrin in the frequency range 100 Hz-10 MHz, was performed on a Dielectric Analyzer 2970 (DEA 2970) instrument (DuPont, USA). The equipment was run by the computer, and for all necessary operations commanding programs were developed working under the operative system TA. Samples were prepared in the form of tablets of 0.7 mm width and radius of 10 mm [7].

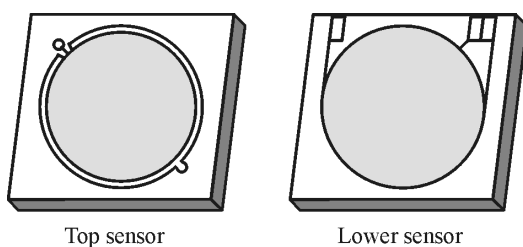


Figure 4. Electrodes of the dielectric analyzer.

Measurement was based on the method of parallel plates, used most in the measurements of the dielectric properties. Two golden electrodes are used, the lower and upper one (Fig. 4.). Electric field was generated by the lower electrode, lying on the heater surface, and which polarized the sample. Platinum temperature detector surrounding the electrode, measured sample temperature and controlled the heater temperature. The upper electrode, fixed to the equipment frame, measured the generated current, which was then converted into the output voltage and amplified. Protective ring about the circle of the upper electrode corrected the dispersion of the electric field and the capacity at the plate edges. Sample widths recorded at the beginning of measurement were used during the experiment to evaluate ϵ' and ϵ'' .

The DEA measures the electric properties of the material as a function of time, tem-

perature and frequency. Measurement is based on two fundamental electric characteristics of the material: capacity and conductivity.

In the dielectric analysis, the sample is placed between two golden electrodes and the sinusoidal voltage alternating electric field is applied. This produces the polarization of the sample, which oscillates with the same frequency as the electric field, but the phase angle is displaced (Fig. 5.). This displacement is measured by comparing the applied voltage and recorded current.

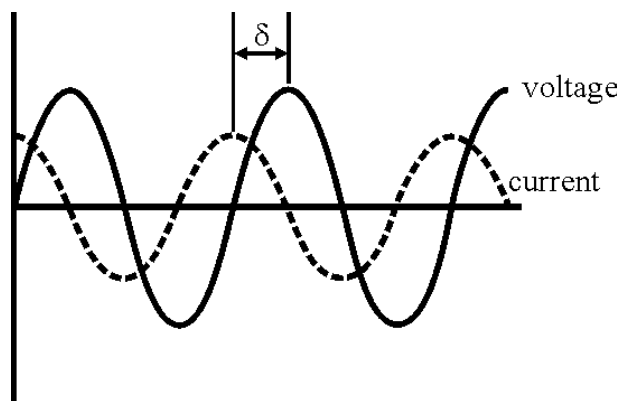


Figure 5. Time dependence of voltage and current between the upper and lower electrode.

Using the measured capacity and conductivity, one can derive the values of :

- a) permittivity (ϵ') - proportional to the capacity measuring the ordering of dipoles;
- b) loss factor (ϵ'') proportional to the conductivity measuring the energy needed for dipole ordering.

3. Results and discussion

3.1. Frequency dependence of the measured quantities

3.1.1. Frequency dependence of the relative dielectric constant of the BCDFe complex

Results presented in Fig. 6. show that at low frequencies the value of dielectric constant falls abruptly, and then decreases slower. One can also notice that the value of dielectric constant decreases with temperature. This happens because of the fact that at very high frequencies the mechanical system can not follow the fast changes of the electric field, meaning that all types of polarization mechanisms vanish. The “response” of the material to extremely high frequencies of the external field is missing. When the field frequency increases towards infinity, the value of relative dielectric constant equals approximately to unity. One can notice at the plot that the value of ϵ' tends towards unity.

The increase in the value of relative dielectric constant with temperature can be ascribed to the fact that the orientational polarization is related to the thermal motion of

the molecules. At low temperatures, the dipoles can not be oriented. When the temperature increases, dipole orientation is enhanced. This increases the value of orientational polarization, causing an increase in the relative dielectric constant.

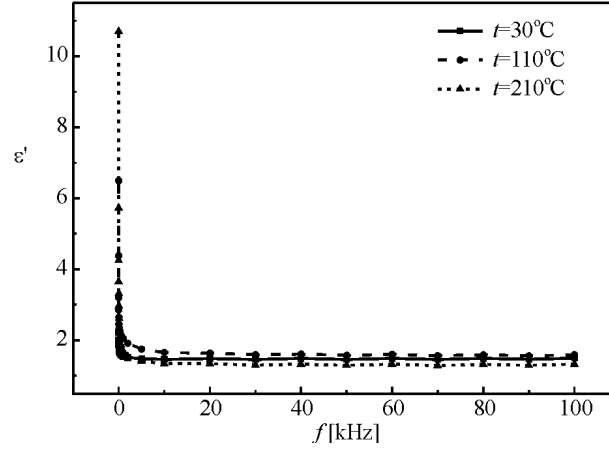


Figure 6. Permittivity dependence on frequency at different temperatures for the complex BCDFe.

3.1.2. Frequency dependence of dielectric losses, $\varepsilon'' = f(\nu)$

One can notice from Fig. 7. that the value of ε'' is constant at low frequencies, while it rises abruptly at high frequencies.

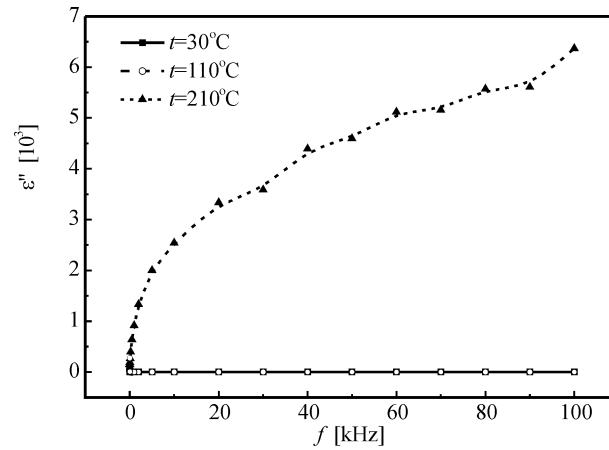


Figure 7. Frequency dependence of dielectric losses at different temperatures for the complex BCDFe.

3.1.3. Frequency dependence of specific conductivity, $\sigma = f(\nu)$

As can be seen from Fig. 8., the increase in frequency yields also the increase in the specific conductivity. One should expect the conductivity increase with rising temperature, and it actually happens, since at higher temperatures molecules are more mobile.

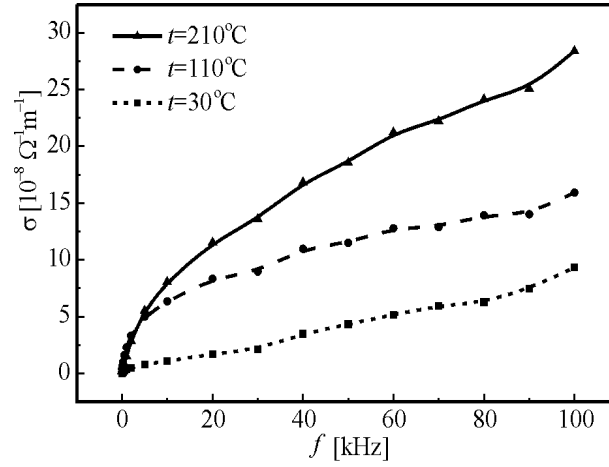


Figure 8. Frequency dependence of specific conductivity at different temperatures for the complex BCDFe.

3.2. Temperature dependence of dielectric properties of the BCDFe complex

3.2.1. Conductivity

The study plot of the dependence of conductivity on temperature, for various frequencies, shows that the conductivity increases with increasing temperature, as expected. For various values of the frequency, which are kept constant for a fixed time period, this rise of conductivity also varies. Generalizing, we can state that this is an approximate exponential dependence.

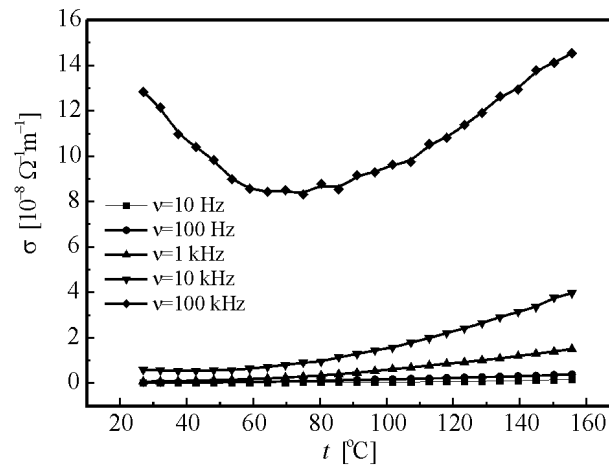


Figure 9. Temperature dependence of conductivity for the complex BCDFe.

However, for the given distribution (Fig. 9.) this does not equally holds for all the values of frequency.

Most pronounced changes occur for the frequency of 100 kHz. Namely, in the temperature range from 20 °C to 70 °C, the conductivity decreases first, and only then increases without any unexpected deviations, indicating that at the given frequency the temperature rise to 70 °C leads to a decrease of conductivity following one mechanism, and above that temperature there occurs conductivity increase, by another mechanism. This might be explained by the nature of the complex. Conductivity values range from $10^{-7} \Omega^{-1} \text{m}^{-1}$ to $10^{-11} \Omega^{-1} \text{m}^{-1}$.

3.2.2. Loss factor

The loss factor rises almost exponentially at lower frequencies (Fig. 10.). Substantial change of loss factor (between 0 and 13 units) for the frequency of 10 Hz points to the dipole character of the material studied and large energy spent for the orientation of these dipoles, increasing with increase in temperature. With increasing frequency, the dipoles can not follow the rate of changes, so that they react to such fields more weakly. It is observed that losses are smaller at higher frequencies. Namely, they decrease with rising frequency and at the given, high frequencies, their variation can be neglected.

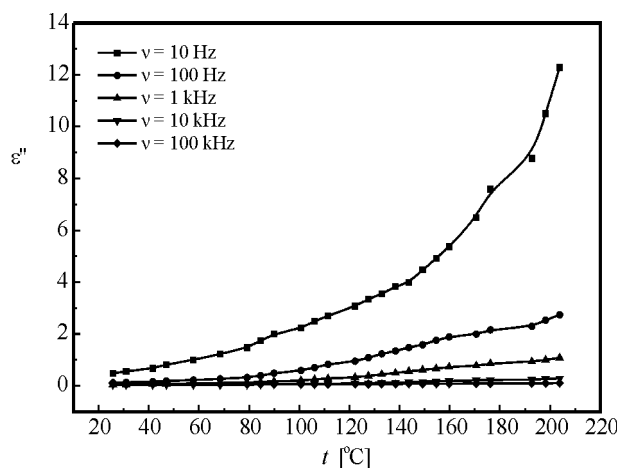


Figure 10. Temperature dependence of loss factor for the complex BCDFe.

3.2.3. Permittivity

As for the permittivity (Fig. 11.), it is not simple to conclude and explain the differences in the behavior at various frequencies. At high frequencies (10 kHz and 100 kHz) the permittivity decreases, while at the lower ones (from 10 Hz to 1 kHz) it increases. The permittivity has values from 2 to 9 (units). The larger value of permittivity at lower frequencies (10 Hz) indicates the existence of dipoles, while the rise with temperatures follows the structural changes indicating aggregation, i.e. a decrease in the number of dipoles above the temperature of 140 °C.

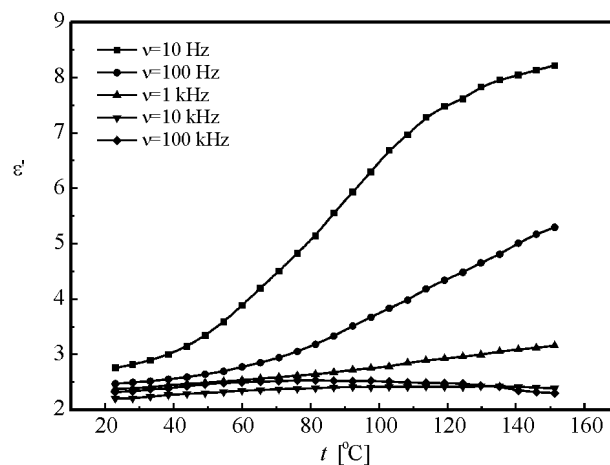


Figure 11. Temperature dependence of permittivity for the complex BCDFe.

3.3. Comparison of dielectric properties between the complex and Fe(II)-fumarate and β -cyclodextrin

The results for the complex were compared with those for pure Fe(II)-fumarate and pure β -cyclodextrin. It is assumed that on the basis of the interpretation of the difference in the same dielectric property one can conclude more about the structure of the molecule, i.e. confirm the inclusion of a certain guest molecule into the host crystal structure (*guest/host* components) [8].

The dependence of the relative dielectric constant, dielectric losses and conductivity on frequency and temperature for Fe(II)-fumarate is given in Figs. 12., 13. and 14. [9,10].

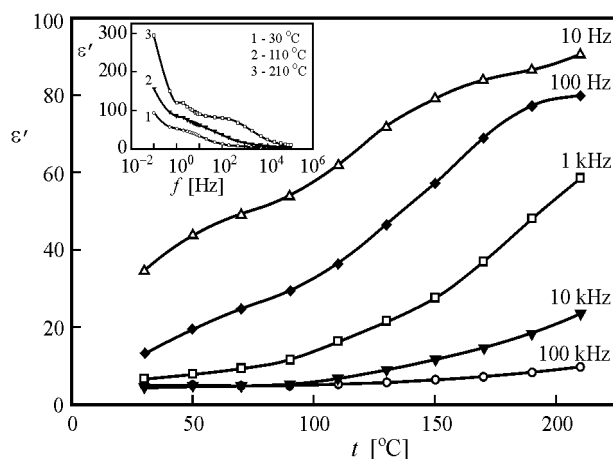


Figure 12. Dependence of dielectric constant on temperature and frequency for Fe(II)-fumarate.

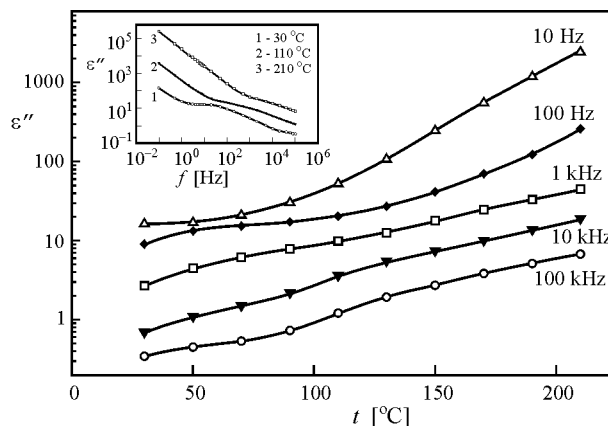


Figure 13. Dependence of dielectric losses on temperature and frequency for Fe(II)-fumarate.

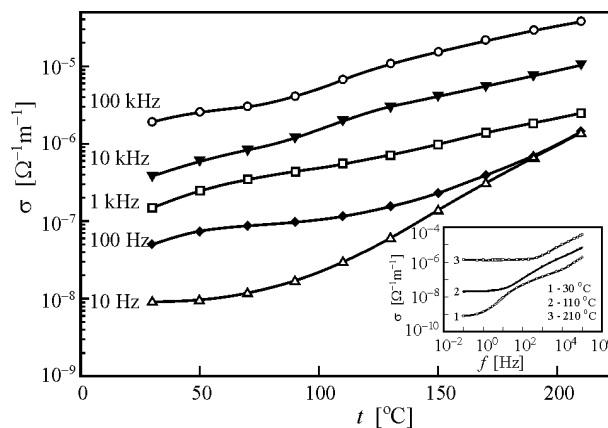


Figure 14. Dependence of specific conductivity on temperature and frequency for Fe(II)-fumarate.

3.3.1. Conductivity

The conductivity of Fe(II)-fumarate increases with frequency. The conductivity of the complex reaches $3 \cdot 10^{-7} \Omega^{-1} \text{m}^{-1}$, while the conductivity of Fe(II)-fumarate ranges up to $10^{-5} \Omega^{-1} \text{m}^{-1}$. This is due to the presence of the iron. Also, the values of conductivity at high frequencies for Fe(II)-fumarate seem to converge to a single value at different temperatures. For the complex it seems that there exist rather large differences in the values of conductivity at high frequencies.

In the case of Fe(II)-fumarate, conductivity rises with rising temperature (as well as frequency), approximately according to an exponential law. This was expected, especially in the range of lower frequencies. The mobility of molecules increases with rising temperature, and so does the conductivity, following an exponential law. The iron, as a typical metal, has a dominant influence on the conductivity of Fe(II)-fumarate.

Such clear case is not found in the complex BCDFe, since the conductivity is influenced only by the iron from Fe(II)-fumarate. Hence, we can notice that the conductivity of the complex is lower by almost two orders of magnitude.

The temperature dependence of conductivity of pure β -cyclodextrin (Fig. 15.), for various frequencies has a very similar trend as in the case of the complex. The conductivity at lower frequencies has a weak exponential rise, while at the frequency of 100 kHz, only from the temperature of about 70 °C (the same as for the complex) the conductivity shows a sudden exponential rise. Conductivity values are of the same order of magnitude as for the complex.

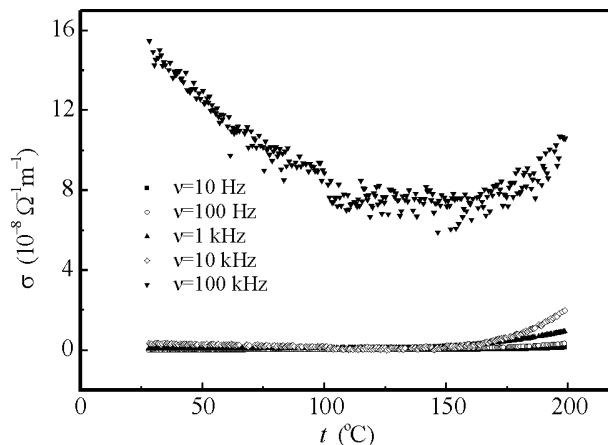


Figure 15. Temperature dependence of conductivity of pure β -cyclodextrin.

3.3.2. Permittivity

Just as for the BCDFe complex, the dielectric constant for Fe(II)-fumarate decreases with increasing frequency, but not so suddenly. The values of ϵ' range from 1 – 11 (units) for the complex, while for ferrofumarate the range is 0 – 300 (units).

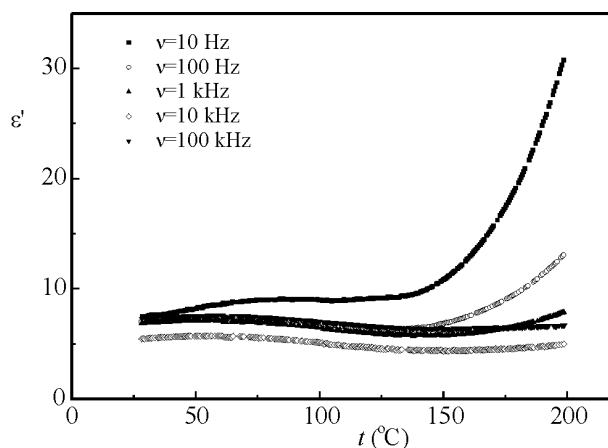


Figure 16. Temperature dependence of permittivity of pure β -cyclodextrin.

The permittivity of pure Fe(II)-fumarate is larger than that for the complex. Besides, we can not observe any decrease with rising temperature at high frequencies, as in the case of complex.

The permittivity of pure β -cyclodextrin (Fig. 16.) at low frequencies rises abruptly with increase in temperature, while at high frequencies it is almost constant or slowly rising. Values of the permittivity range somewhere between the values for the complex and values for pure ferrofumarate, i.e. from 5 to 30, although they are closer to the value for the complex.

3.3.3. Loss factor

Dielectric losses for Fe(II)-fumarate decrease with increase in frequency, while for the in complex they decrease at 210 °C, and at lower temperatures they are constant.

The loss factor for pure Fe(II)-fumarate is much higher, and constantly increases with increasing temperature. The tendency of an exponential growth of the loss factor is asimilar for the complexes and pure Fe(II)-fumarate. The loss factor (Fig. 17.) of pure β -cyclodextrin has a similar tendency as for the complex (i.e. increases with increasing temperature, much faster at lower frequencies), but its values are substantially lower, being only 0.15 (unit).

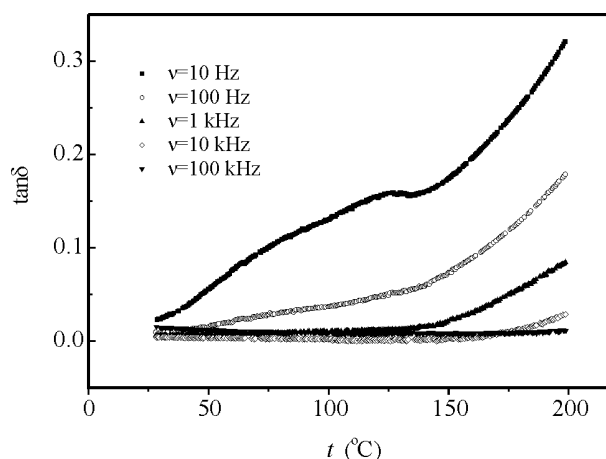


Figure 17. Temperature dependence of loss factor of pure β -cyclodextrin.

4. Conclusion

The dielectric constant, as well as the loss factor for all samples decreases with frequency. The basic trend of these quantities with increase in temperature is a mild rise of the value, which in the vicinity of the melting point begins to rise abruptly. The conductivity of the complex of $10^{-7} \Omega^{-1} \text{ m}^{-1}$ corresponds approximately to the results for BCD, while for the Fe(II)-fumarate it is by two orders of magnitude higher. At the frequency of 10 Hz, the permittivity for the complex and BCD shows a similar behaviour with respect to temperature increase, with an inflection point observed in the temperature range of 80 °C–90 °C for BCD, while for the complex it appears in the range of 110 °C–120 °C. The same variation in the same temperature range is also noticed for the loss factor, indicating that the increase of the value of the energy spent for the dipole orientation is in the complex activated at higher temperature and has somewhat higher value (2.0 unit)

than for BCD (0.15 unit), while the loss factor for pure Fe(II)-fumarate (20 – 30 unit) is substantially higher.

The obtained results indicate similar dielectric behavior of the complexes and BCD, as it could be expected in the case of formation of host-guest inclusion complex. Small differences can be ascribed to higher inertness of the molecules of the complex with the frequency of applied field, taking into account the realized inclusion.

Such study of powder materials makes it possible to confirm the complexation, since the studied complex loses the expressed conductivity properties of Fe(II)-fumarate and behaves dielectrically as the host compound, i.e. BCD.

Acknowledgments

The authors thank Dr Vesna Nikolić from the Faculty of Technology in Leskovac for the materials and preparation of the inclusion complex. This work was supported by the Ministry of Science and Technological Development of the Republic of Serbia, Project No. 142059.

References

- [1] K. H. Frömming, J. Szejtli (Eds.), *Cyclodextrins in Pharmacy*, (Kluwer, Dordrecht, 1994.).
- [2] W. Saenger, *Angew. Chem. Int., Ed. Engl.* **19**, 344 (1980).
- [3] T. Steiner, G.Koellner, *J. Am. Chem. Soc.* **116**, 5122 (1994).
- [4] L. Hallberg, H. G. Harwerth, A. Vannotti, *Iron Deficiency*, (Academic Press, London and New York, 1970).
- [5] D. M. Cvetković, V. D. Nikolić, Lj. B. Nikolić, *CI&CEQ* **11**, No.1, 30 (2005).
- [6] L. Liu, S. Zhu, *J. Pharm. Biomed. Anal.* **40**, 122 (2006).
- [7] Z. Cvejić, S. Rakić, S.Jankov, S. Skuban, A. Kapor, *Journal of Alloys and Compounds* **480**, 2, (2009).
- [8] A. Kapor, S. Skuban, V. Nikolić, Ž. Cvejić, S. Rakić, *Journal of Research in Physics* **32**, No.1, 25 (2008).
- [9] S. J. Skuban, T. Džomić and A. Kapor, *International Journal of Modern Physics B*, (accepted on May 21, 2008.).
- [10] S. J. Skuban, T. Džomić and A. Kapor, *AIP Conference. Proceedings* **899**, 652 (2007).

Deuterium Production as a Possible Tool for Estimation of the Thermal Neutron Fluence in the Low-background Ge-detector

N. Jovančević, M. Krmar, J. Slivka, D. Mrdja, I. Bikit
*University of Novi Sad, Faculty of Science, Department of Physics,
Trg Dositeja Obradovica 4, 21000 Novi Sad, Serbia*

Received: December 18, 2009

Abstract

If bulk sample measured in some low background gamma spectroscopy system contains hydrogen, neutrons produced by cosmic muons in the shield and other surrounding materials can be captured. High energy photon (2223 keV) is emitted in the process of deuterium production. Intensity of the 2223 keV line in measured gamma spectra was used to estimate thermal neutron flux in detector vicinity. The obtained results are compared with values of thermal neutron flux obtained using the gamma lines emitted after the neutron capture in Ge.

Key words: gamma spectroscopy, deuterium production, neutron captures, thermal neutron flux

1. Introduction

Nuclear and particle physics, astrophysics, geophysics, life and environmental sciences, and some other areas use low-level, high resolution Ge-spectroscopy. A most important requirement of the very sensitive equipment and sophisticated data acquisition systems is to be capable to discriminate desired events from all kinds of background. Background reduction is sometimes the only possible way to improve sensitivity of the experiment [1-7].

At the sea level, natural radioactivity is most important source of background in Ge gamma spectroscopy. The dominant component of background is gamma radiation emitted by natural radionuclides. It can be reduced by passive shield. Thickness of 15 cm of radio-impurities free lead can reduce natural radioisotope background by about four orders of magnitude. Another significant source of background are neutrons. There are two sources of neutrons associated with local natural radioactivity: neutrons produced via (α, n) reactions and spontaneous fission of U and Th [8]. Both groups of neutrons have low energy in MeV energy region [10].

After elimination of gaseous Rn and daughter nuclei and reduction of external natural radiation by the massive shield, the most significant source of background is cosmic radiation [11]. It can be roughly divided to two most important components: muons identified by high energy deposition in detector crystal and neutrons produced by cosmic-ray muons. Cosmic neutrons can be created through several processes: muon capture, usually

at the sea level or in shallow depths, muon-induced spallation reactions, hadron nuclear reactions and photonuclear reactions [12,13]. The energy of these neutrons can be even in GeV energy region. It is shown [14,15] that neutron production rate by the cosmic muons increases with the atomic weight of material. This means that common passive lead shield turns into source of neutrons.

Activity induced by neutron capture in shielding and all other surrounding materials, as well as in the detector itself, is another important source of background. Characteristic gamma lines following thermal capture and inelastic scattering in Ge nuclides can identify neutrons, both terrestrial and those produced by cosmic radiation. Estimation of neutron flux in gamma spectroscopy systems can be done by interaction of neutrons with germanium itself. Gamma lines at the energies of 139.9 keV and 198.4 keV appear in the spectra as a result of thermal neutron capture by ^{74}Ge and ^{70}Ge , respectively [7]. Two broad and asymmetric peaks in the spectra at 596 keV and 691.3 keV result from inelastic neutron scattering ((n,n') reaction) on ^{74}Ge and ^{72}Ge , respectively, and can be used for estimation of fast neutron flux [16].

The common case (in environmental sciences especially) is that bulk samples in Marinelli geometry are used to improve detection efficiency. If measured sample contains hydrogen, creation of deuterium through the $^1\text{H}(n,\gamma)^2\text{H}$ nuclear reaction can occur. Emission of the 2223 keV photon follows capture of thermal neutron on hydrogen nuclei. This means that the presence of thermal neutrons can be recognized by analyzing the 2223 keV peak in the spectra. In order to explore the potential use of the $^1\text{H}(n,\gamma)^2\text{H}$ nuclear reaction and 2223 keV gamma line in possible estimation of neutron flux in detector vicinity, several different materials containing hydrogen were packed in Marinelli geometry and long spectra (order of magnitude 1000 ks) were recorded. Flux of thermal neutrons is estimated by the use of gamma radiation emitted after neutron capture in ^{74}Ge and ^{70}Ge , as well as after capture in ^1H .

2. Experimental setup

Low background HPGe detection systems were used for measuring the activity induced by the interaction of neutrons with different materials which surround the detectors. Large-volume germanium spectrometer, made by Canberra, is located on the basement of the Department of Physics in Novi Sad. It has 100% relative efficiency, which corresponds to about 380 cm^3 of detector active volume. The detector shield is constructed with layered bulk lead. The total mass of the lead shield is 1633 kg. The lining materials are low-background tin thickness of 1 mm, and high purity copper thickness of 1.5 mm. The shield is equipped with a gas port for the introduction of nitrogen from the Dewar vessel to flush the shield interior in order to reduce the background from radon and radon descendants.

Two different materials were packed in a PVC Marinelli container: $\text{CuSO}_4 \cdot 5\text{H}_2\text{O}$ and paraffin. Both materials are non-expensive and accessibly in amounts to fill the large Marinelli container. The measurement time when $\text{CuSO}_4 \cdot 5\text{H}_2\text{O}$ was around the detector was 3434419 s. Total mass of $\text{CuSO}_4 \cdot 5\text{H}_2\text{O}$ powder was 5.847 kg. It can be expected that CuSO_4 with 5 molecules of water should be efficient in slowing-down neutrons. In second measurement, the Marinelli container was filled by melted paraffin, very rich in hydrogen, acting as a very strong moderator around the HPGe detector. Total mass of paraffin was 2.210 kg and the time of measurement was 3941023 s.

3. Results

3.1. Neutron capture in hydrogen

In both spectra, measured with $\text{CuSO}_4 \cdot 5\text{H}_2\text{O}$ and paraffin around the detector, prominent 2223 keV gamma line appeared. Figure 1 shows high energy part of the spectrum measured with paraffin where 2223 keV gamma line can be seen. In the background spectrum taken without surrounding materials the mentioned line was never observed. The absence of 2223 keV gamma line in the spectra measured with materials having no hydrogen (as NaCl for example) in the Marinelli container was observed.

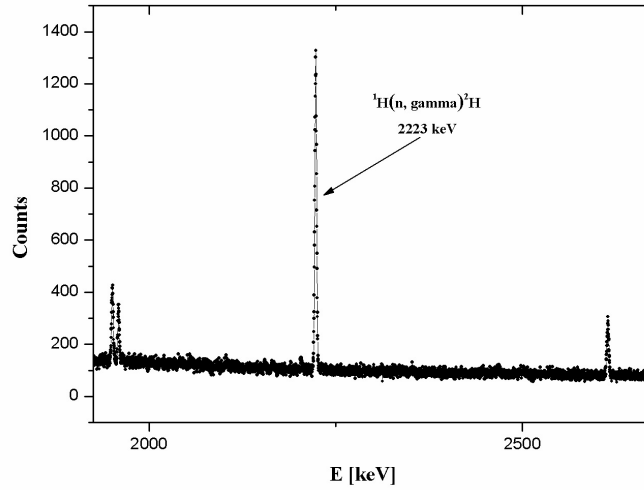


Figure 1. High-energy part of the spectrum recorded with paraffin around the detector.

Characteristic count rate of 2223 keV photons was 2.86 (8) counts/ks for $\text{CuSO}_4 \cdot 5\text{H}_2\text{O}$ and 5.3 (1) counts/ks for paraffin. The flux of thermal neutrons can be estimated using the intensity of the 2223 keV gamma line. The flux was calculated by the following expression:

$$\Phi = \frac{I}{\sigma \cdot \varepsilon \cdot N_{\text{H}}}. \quad (1)$$

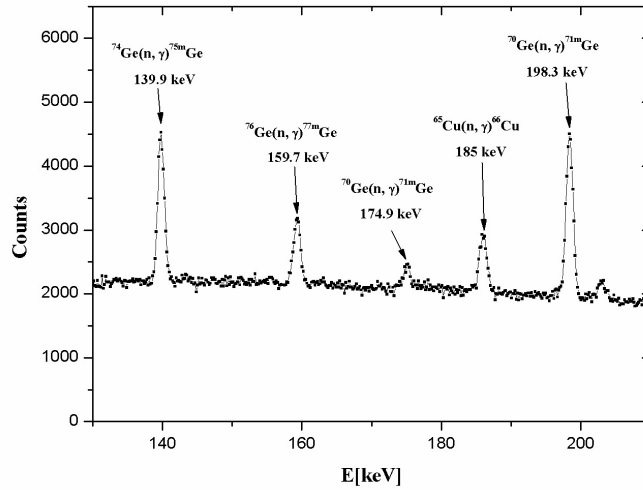
where I is the intensity of the observed gamma line; σ is the cross-section for neutron capture; ε is the total efficiency for detection of 2223 keV photons, and N_{H} is the number of hydrogen atoms in the detector surrounding. The detection efficiency for the gamma photons was estimated by a Geant4 [17] simulation. In the simulation, the 2223 keV gamma photons were randomly created in the volume of Marinelli container. It was obtained that total detection efficiency for $\text{CuSO}_4 \cdot 5\text{H}_2\text{O}$ was $8.2(2) \cdot 10^{-3}$. Penetration abilities of the 2223 keV photons through paraffin are slightly higher, so that the total efficiency was $12.2(2) \cdot 10^{-3}$. Total number of hydrogen atoms in $\text{CuSO}_4 \cdot 5\text{H}_2\text{O}$ was $1.41 \cdot 10^{26}$, while in paraffin it was $1.96 \cdot 10^{26}$. The cross-section for thermal neutron capture on ^1H was 0.332 barn. Calculated values of thermal neutron flux are presented in Table 1.

Table 1. Flux of thermal neutrons measured by capture in hydrogen and Ge.

Material surrounding the detector	Φ_T [$s^{-1} m^{-2}$] H	Φ [$s^{-1} m^{-2}$] Ge
CuSO ₄ · 5H ₂ O	75.3 (27)	45 (7)
Paraffin	69.4 (18)	58 (9)

3.2. Neutron capture in Ge

The number of gamma lines following de-excitation of Ge nuclei after neutron capture appeared in the spectrum recorded using the detector shielded with lead. The low-energy part of spectrum obtained with CuSO₄ · 5H₂O around the detector, presented in Figure 2, shows several well known gamma lines including the most intensive ones 139.5 keV ($^{74}\text{Ge}(n, \gamma)^{75m}\text{Ge}$) and 198.3 keV ($^{70}\text{Ge}(n, \gamma)^{71m}\text{Ge}$). Count rates of the 139.5 keV photons emitted after neutron capture was 4.61 (7) counts/ks with CuSO₄ · 5H₂O around the detector and 5.85 (6) counts/ks with paraffin-surrounded detector.

**Figure 2.** Part of the spectrum collected by the Ge detector. The detector was surrounded by CuSO₄ · 5H₂O in a Marinelli container.

It is possible to estimate the value of thermal neutron flux at the site of the detector using intensity of the 139.9 keV gamma line produced in the interaction of neutrons with Ge. The thermal neutron flux was estimated by the expression [16]:

$$\Phi_T = \frac{980 I_{139.9}}{(\varepsilon_{139.9}^\gamma + 1.6) V}, \quad (2)$$

$$\varepsilon_{139.9}^\gamma \approx 1 - \frac{1 - e^{-V^{-1/3}}}{V^{1/3}}, \quad (3)$$

where $I_{139.9}$ is the count rate in s^{-1} of the 139.9 keV line, and V is the volume of detector in cm^3 . Volume of the HPGe detector used in experiment was $V = 380 cm^3$.

The flux of thermal neutrons in the detector was calculated when $CuSO_4 \cdot 5H_2O$ and paraffin are present in the surroundings of the detector. The obtained results are presented in Table 1.

4. Conclusion

In the measurement geometries where the bulk sources containing hydrogen are located in a gamma spectroscopy system, the 2223 keV line following creation of deuterium can be used to estimate the thermal neutron flux at the detector place. This method has some advantages over standard neutron detection using ^{75m}Ge gamma line of 139.9 keV. The ^{75m}Ge method is based on Equation (2), containing an empirical term ranging from 300 to 1000. The neutron flux determined using the 2223 keV gamma line, does not employ empirical factors. Possible source of systematic uncertainty can be the efficiency of the detection system. The multiplicative parameter in the numerator in Equation (2) is usually determined with higher uncertainty than the statistical error of the 2223 keV gamma line. This means that the overall uncertainty of the result obtained using the hydrogen capture is lower than that of the result obtained by activation of Ge.

Comparison of the values obtained by two different methods shows some differences. It can be seen that the values of thermal neutron flux obtained by the use of deuterium creation are higher than the values obtained by neutron capture in ^{74}Ge nucleus. Besides, the use of the 2223 keV line gives that the thermal neutron flux in $CuSO_4 \cdot 5H_2O$ is higher than the neutron flux in paraffin. Neutron flux estimated using activation of ^{74}Ge nuclei shows an opposite trend: there are more neutrons when paraffin is wrapped around the detector. Possible reasons for the observed difference between two methods should be analyzed. It should be checked if the distribution of thermal neutrons is uniform over the area of detector and sample packed in the Marinelli container. It can be possible that the hydrogen atoms in the container and in Ge crystal are not exposed to an identical number of neutrons.

References

- [1] G. Heusser, Background in ionizing radiation detection, In: Garcia-Leon, M., Garcia-Tenorio, R. (Eds.), *Low-Level Measurements of Radioactivity in the Environment*. Word Scientific, Sigapore, pp. 69-112. (1994).
- [2] G. Heusser, *Annu. Rev.Nucl. Part. Sci.* 1995. 45:543-90.
- [3] P. P. Povinec, Underground low-level counting. In: Garcia-Leon, M., Garcia-Tenorio, R. (Eds.), *Low-Level Measurements of Radioactivity in the Environment*. Word Scientific, Sigapore, pp. 113-140. (1994).
- [4] P. P. Povinec, Developments in analytical technologies for marine radionuclide studies. In Livingston, H. D. (Ed.), *Marine Radioactivity*. Elsevier, Amsterdam, pp. 237-294, (2004).

-
- [5] I. Zvira, P. P. Povinec, I. Sykora, Determination of very low levels of radioactivity. *Pure Appl. Chem.* **66(12)**, 2537-2586, (1994).
- [6] R. Wordel, et al., Study of neutron and muon background in low-level germanium gamma-ray spectrometry, *Nucl. Instr. and Meth. A* **369**, 557-562 (1996).
- [7] G. Heusser, Cosmic ray interaction study with low-level Ge-spectrometry, *Nucl. Instr. and Meth. A* **369**, 539-543 (1996).
- [8] Y. Feige, B. G. Olman, J. Kastner, Production rates of neutrons in soils due to natural radioactivity, *J. Geophys. Res.* **73**, 3135-3142 (1968).
- [9] G. Heusser, Progress in Ge-spectrometry at the Max-Planck-Institut für Kernphysik Heidelberg, In: Povinec P. (Ed.), *Rare Nuclear Processes*, World Scientific, Singapore, pp. 247-255 (1992).
- [10] NCRP Report Nr. 94. Exposure of the Population in the United States and Canada from Natural Background Radiation (National Council on Radiation Protection and Measurement, Bethesda, 1987).
- [11] T. Geiser, *Cosmic Rays and Particle Physics*, Cambridge Univ. Press., Cambridge (1990).
- [12] A. Da Silva et al., *Nucl. Instrum. and Meth. In Phys. Res. A* **354**, 553 (1995).
- [13] V. A. Kudryavtsev, N. J. C. Spooner and J. E. McMillan, *Nucl. Instrum. and Meth. In Phys. Res. A* **505**, 688 (2003).
- [14] Stephen Croft, Ludovic C.A. Bourva, *Nucl. Instrum. and Meth. In Phys. Res. A* **505**, 536-539 (2003).
- [15] R. J. Arthur, J. H. Reeves, H. S. Miley, Use of low-background germanium detectors to pre-select high purity materials intended for construction of advanced ultra low-level detectors, *IEEE Trans. Nucl. Sci.*, 582-585 (1988).
- [16] G. P. Skoro, I. V. Anicin, A. H. Kukoc, Dj. Krmpotic, P. Adzic, R. Vukanovic and M. Zupancic, *Nucl. Instrum. and Meth. In Phys. Res. A* **316**, 333 (1992).
- [17] S. Agostinelli et al., (GEANT4 Collaboration). *Nucl. Instrum. and Meth. In Phys. Res. A* **506**, 250 (2003).

Analysis of Some Dielectric Parameters of the $\text{Bi}_6(\text{As}_2\text{S}_3)_{94}$ Glass

M.V. Šiljegović¹, S.R. Lukić-Petrović^{1*}, M. Slankamenac², R.V. Kisić¹,
A.S. Tveryanovich³

¹*University of Novi Sad, Department of Physics, Faculty of Sciences,
Trg Dositeja Obradovica 4, 21000 Novi Sad, Serbia*

²*University of Novi Sad, Faculty of Technical Sciences, Novi Sad, Serbia*

³*Department of Chemistry, St. Petersburg State University, Universitetskiy pr. 26,
St. Petersburg 198504, Russia*

Received: December 23, 2009

Abstract

The paper describes a study of the frequency dependence of some dielectric parameters in the frequency range from 1 kHz to 1 MHz for the $\text{Bi}_6(\text{As}_2\text{S}_3)_{94}$ glass at different temperatures. The results obtained are interpreted in terms of the Debye theory of molecular dipoles, and they indicate the existence of different types of dipoles that determine the mechanism of dielectric behavior of the investigated glass. By analyzing Cole-Cole diagrams, several dispersion parameters were determined that describe the occurrence of dielectric relaxation in the low- and high-temperature range. Using the Eyring theory of chemical reaction rate, the enthalpy ΔH and activation energy ΔF of the dipole relaxation were determined.

Key words: polarisation, chalcogenides, defect states, relaxation time, Cole-Cole diagrams

1. Introduction

Modifications of the already well-known chalcogenide glasses, like the As-S system, by doping with metal atoms, have been a subject of intensive research in the last decades because of the possibility of preparing materials with specific optical, electrical and physico-chemical properties [1-4]. The Bi-As-S system is interesting not only because of the possibility of changing the type of conductivity at a certain concentration of Bi atoms in the amorphous matrix, but also because of the significant effect on the values of particular physical parameters, already at low concentrations of the dopant metal atoms [5]. Previous studies [6,7] have shown that in the system $\text{Bi}_x(\text{As}_2\text{S}_3)_{100-x}$ ($x < 10$) the glass with $x = 6$ at.% Bi represents a limiting composition since higher Bi concentrations result in a discontinuous behavior of the values of physical parameters (conductivity, transparency,

*Corresponding author: svetlana@df.uns.ac.rs

structural orderliness, etc.). Study of the dielectric properties of this glass provides information about its structure, which is indispensable for the understanding of the conduction mechanism.

The dominant type of polarization established by introducing the glass in a DC or AC electric field depends on the type of structural units and character of the chemical bonds between them, as well on the frequency. For the chalcogenide glasses with the prevailing covalent bonds the main polarization mechanisms are dipole and electronic polarizations. The dielectric behavior of these glasses can be considered in the light of the Debye theory of molecular dipoles [8], which deals with the responses of polar molecules in an AC field. The greatest advantage of this theory is that it enables the determination of molecular polarizability as a characteristic of a particular molecule on the basis of its dielectric constant as the property of the material as a whole.

2. Experimental

The determination of the parameters that describe dielectric behavior of the investigated glass $\text{Bi}_6(\text{As}_2\text{S}_3)_{94}$ was carried out on the basis of the results of measurement on a HP 4194A Impedance/Phase Gain Analyzer instrument. To that end, the thermogenic resistance and capacitance were measured for the sample-holder system at selected temperatures in the range from room temperature to a value close to the phase transition temperature, in the frequency range from 1 kHz to 1 MHz.

To calculate the components of dielectric permittivity ε' and ε'' of the investigated glass use was made of the scheme of parallel connection of a capacitor and a thermogenic resistor, which, in accordance with the semiconducting character of chalcogenide glasses, is most often used for modeling and describing dielectric properties.

In view of the fact that the system sample-holder is equivalent to a system of two parallelly connected capacitors, a correction of the results was made to eliminate the effect of the air capacitor. The real and imaginary parts of the dielectric permittivity were calculated from the following relations:

$$\varepsilon' = \frac{C_{\text{sample}}}{C_0}, \quad (1)$$

$$\varepsilon'' = \frac{1}{R\omega C_0}, \quad (2)$$

where C_{sample} and C_0 are the respective capacitors of the sample and holder, ω is the field frequency, and R is the thermogenic resistance.

3. Results and Discussion

The frequency-temperature dependence of the dielectric constant for the $\text{Bi}_6(\text{As}_2\text{S}_3)_{94}$ glass (Figure 1) is in concordance with the Debye theory of molecular dipoles, and hence this theory can be used for the interpretation of the experimental results. The origin of molecular dipoles in glasses involving Bi is associated with charged defect states [9], structural micro-inhomogeneity, high polarizability of Bi atoms [10], and formation of microclusters [11].

The temperature behavior of the dielectric constant is explained by the fact that the orientational polarization is a function of thermal rate of molecules, i.e. by the limited ability of the orientation of dipoles at low temperatures due to the occurrence of rotational degrees of freedom [12,13].

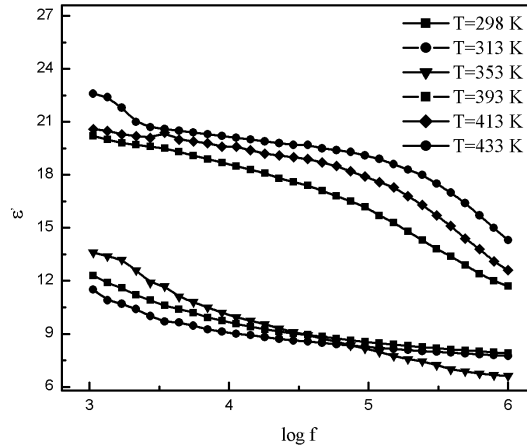


Figure 1. Dispersion of the dielectric constant for the $\text{Bi}_6(\text{As}_2\text{S}_3)_{94}$ glass at different T .

The dispersion of the dielectric constant in the measured frequency interval (Figure 1) is a consequence of hindered orientation of dipoles in the direction of the field with respect to the other possible directions because of the more frequent changes of the direction of the field at higher frequencies. This effect is also manifested as an increase in the imaginary component of the dielectric permittivity for the first three temperatures (Figure 2).

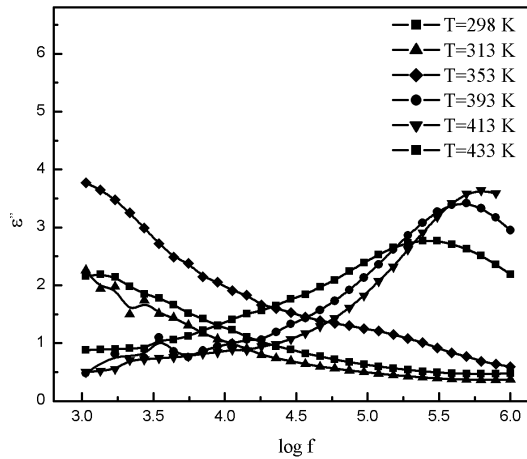


Figure 2. Dispersion of the loss factor for the $\text{Bi}_6(\text{As}_2\text{S}_3)_{94}$ glass at different T

The higher value of the loss factor can be also interpreted by the increase of conductivity of the lagging and absorbed currents. However, for the remaining three temperatures from the selected T interval this parameter changes its slope and exhibits a maximum at high frequencies, which indicates that the other types of molecular dipoles are dominantly responsible for the dielectric behavior of the investigated material in the high-temperature range. This conclusion also suggests the observation that the values of the dielectric

constant are significantly higher at these temperatures compared to the low-temperature values (Figure 1).

In view of their amorphous character, chalcogenide glasses possess charged defect states [14], so that at lower temperatures dominate the dipoles of the so-called valence alternating pairs, formed by the electron transfer from one chalcogenide atom to another [11]. Also, it is known that *Bi* enters the amorphous matrix as a charged impurity [15,16,17], a consequence of this being not only the increase in the number of alternating pairs but also of the change of their equilibrium in the sense of conversion of the particular D^+ to D^- states. At high temperatures, the excitation of these centers and formation of neutral defect centers take place, which can be considered responsible for the dielectric properties of the $\text{Bi}_6(\text{As}_2\text{S}_3)_{94}$ glass in the high-temperature range.

The dielectric losses in the glass exposed to thermal treatment originate from three contributions: thermally activated relaxation of freely rotating dipoles of Debye type, electric conductivity due to electron-phonon interactions, and vibrational losses [18].

The proportion of the losses due to the Joule effect was estimated from the relation [19-21]:

$$\varepsilon''_{\text{DC}} = \frac{\sigma_{\text{DC}}}{\omega\varepsilon_0}, \quad (3)$$

and presented in Figure 3 for 1 kHz, since heat losses are significant only at low frequencies. Although they increase with increase in temperature, their numerical values compared to the overall losses for the $\text{Bi}_6(\text{As}_2\text{S}_3)_{94}$ glass (Figure 2) are negligibly small, so that it can be concluded that dielectric losses are primarily originated from the dipole mechanism.

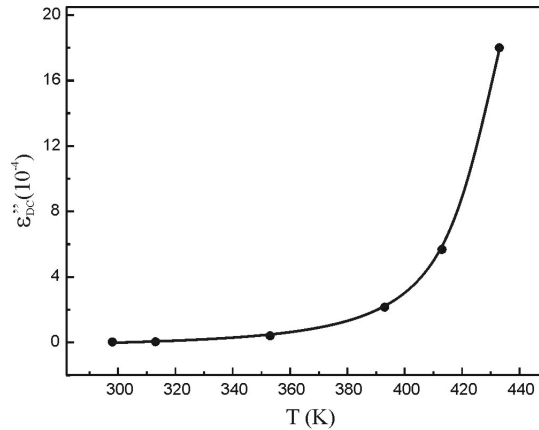


Figure 3. Temperature dependence of the DC factor of losses for the $\text{Bi}_6(\text{As}_2\text{S}_3)_{94}$ glass at 1 kHz.

In accordance with the Debye theory, a characteristic of dipole losses is that they exhibit a maximum at a certain temperature. Namely, the effects of the increase in temperature and decrease in viscosity, each in its turn, influence the amount of losses, so that the degree of dipole orientation increases simultaneously with decrease in the energy needed for overcoming the resistance of the viscous medium, and, while the former effect increases the slope of the losses, the latter has an opposite effect.

The frequency ω' that corresponds to the maximum of losses at the given temperature (Figure 4) represents the resonance frequency at which the period of the external electric

field coincides with the dipole relaxation time needed to overcome the resistance of the viscous medium.

From the approximate condition:

$$\omega\tau = 1, \quad (4)$$

which holds for polar dielectrics it is easy to calculate the numerical values for dipole relaxation times at the given temperature (Table 1). The obtained values are characteristic for amorphous chalcogenides [22-24].

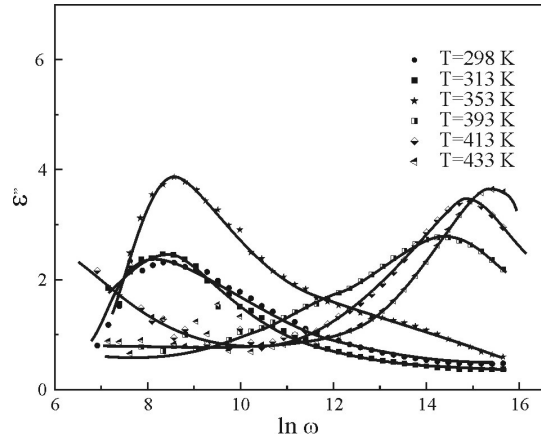


Figure 4. Dependence of the factor of losses on the frequency logarithm for the $\text{Bi}_6(\text{As}_2\text{S}_3)_{94}$ glass.

The different positions of the maxima in Figure 4 indicate not only the existence of two dipole types in different temperature intervals but also the distribution of relaxation times.

By analyzing the Debye theory, Cole and Cole [25] found that the values of real and imaginary parts of the dielectric permittivity for different frequencies in the dispersion area lie on a semi-circle, i.e. the relation between these two parameters can be expressed as:

$$\left(\varepsilon' - \frac{\varepsilon'_0 + \varepsilon'_\infty}{2}\right)^2 + (\varepsilon'')^2 = \left(\frac{\varepsilon'_0 - \varepsilon'_\infty}{2}\right)^2, \quad (5)$$

where ε'_0 and ε'_∞ are the static and optical dielectric constants, respectively.

The advantage of such presentation of results is the possibility of determining a number of dielectric parameters on the basis of the values that can be read from the Cole-Cole diagram.

Figure 5 shows the Cole-Cole diagrams for $\text{Bi}_6(\text{As}_2\text{S}_3)_{94}$ obtained for particular temperatures. The experimental data deviate to some extent from the Debye theory in the sense that the points lie somewhat below the abscissa and not on it itself, which is characterized by the parameter α , and corresponds to the distribution of dipole relaxation times. This phenomenon is ascribed to the structural complexity of the amorphous material in the sense of the existence of different types of structural units [26, 27].

The macroscopic relaxation time can be determined from the relation:

$$u \cdot \nu = (\omega\tau_0)^{1-\alpha}, \quad (6)$$

where u and ν are the distances from an arbitrarily chosen experimental point on the semi-circle and the static/optical dielectric constant. The calculated values are given in Table 1.

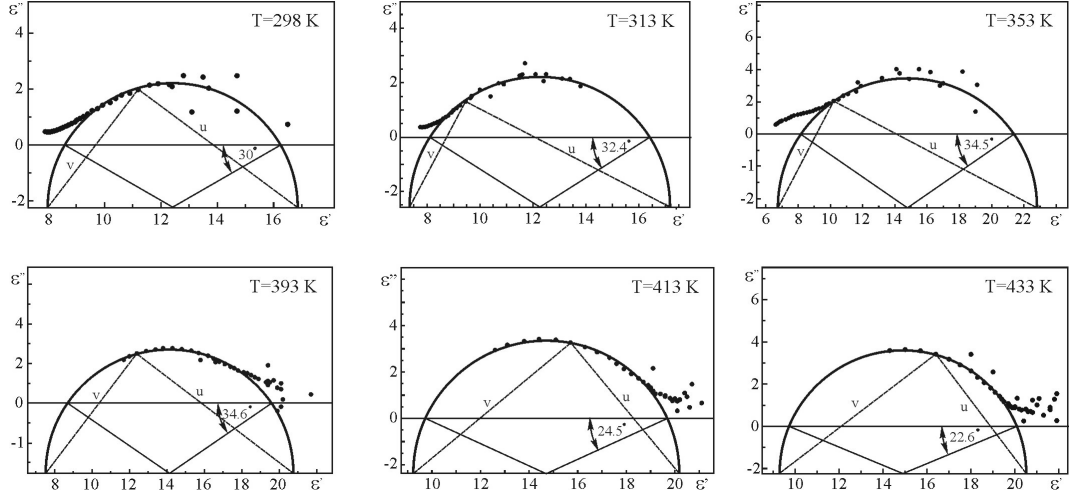


Figure 5. Cole-Cole diagrams for the $\text{Bi}_6(\text{As}_2\text{S}_3)_{94}$ glass at different temperatures.

In that case, the macroscopic dipole relaxation time is determined by the relation:

$$\tau = \tau_0 \left(\frac{2\varepsilon'_0 + \varepsilon_\infty}{3\varepsilon'_\infty} \right) \quad (7)$$

The decrease in relaxation times with temperature in both temperature regions is in concordance with the concept of dipolar relaxation and corresponds to the decrease in intermolecular interactions with increase in thermal energy. The difference of the obtained values by three orders of magnitude in the two regions confirms the previous conclusion about the different nature of the dipoles responsible for the dielectric behavior of the treated sample. Also, it should be noted that there is a good agreement between the values of relaxation times determined from the Cole-Cole diagrams and those determined from the relation (4).

According to the Eyring theory of chemical reaction rate [28], the free activation energy ΔF and enthalpy ΔH of dipole relaxation can be calculated from the temperature dependence of the logarithm of the relaxation time expressed as:

$$\tau = \left(\frac{h}{kT} \right) \exp \left(\frac{\Delta F}{RT} \right) \quad (8)$$

where h , k and R are the Planck, Boltzmann and gas constants, respectively, and $\Delta F = \Delta H - T\Delta S$ (S represents the entropy of the system). The calculated values are presented in Table 1.

The higher values of activation energy of dipole relaxation compared to the activation energy of DC conductivity [6] indicate the domination of the relaxation mechanism of dipole type.

Table 1. Dispersion parameters: α - deviation parameter, τ and τ_0 - macroscopic and microscopic relaxation times, ΔH - enthalpy, ΔF - activation energy .

T (K)	α	τ_0 (10^{-4} s)	τ (10^{-4} s)	ΔH (kcal/mol)	ΔF (kcal/mol)	$\tau = (\omega_M)^{-1}$ (10^{-4} s)
298	0.17	1.11	1.93		12.4	2.30
313	0.18	0.80	1.66	1.67	12.9	2.10
353	0.19	0.51	1.33		14.5	1.88
393	0.19	0.0039	0.0086		12.3	0.0056
413	0.14	0.0040	0.0072	6.25	12.8	0.0034
433	0.125	0.0023	0.0041		13.0	0.0021

4. Conclusion

Dispersion of the real and imaginary parts of the dielectric permittivity of the investigated glass $\text{Bi}_6(\text{As}_2\text{S}_3)_{94}$ is in concordance with the predictions of the Debye theory of molecular dipoles. The results also indicate the existence of the distribution of dipole relaxation times, as well as the different origins of dipoles in the low- and high-frequency regimes. It was found that the polaron mechanism is responsible for the significant increase in the dielectric constant at higher temperatures. The change in the mechanism influences the position of the maximum of the losses in the frequency range, but not on its absolute value. The analysis of the Cole-Cole diagrams yielded the distribution parameters that reflect more closely the dipolar type of relaxation that is responsible for the dielectric behavior of the $\text{Bi}_6(\text{As}_2\text{S}_3)_{94}$ glass.

Acknowledgments

The work is done as part of the Project No. 141026 “*Amorphous and Nanostructural Chalcogenides*”, supported by the Ministry of Science and Technological Development, Republic of Serbia and Project “*Technology of obtaining and characterization of disordered semiconductors*” supported by the Provincial Secretariat of Science and Technological Development, Autonomous Province of Vojvodina.

References

- [1] T. Usuki, O. Uemura, S. Konno, Z. Kameda, J. Non-Cryst. Solids **293-295**, 799, (2002).
- [2] M. Mitkova, M.N. Kozicki, J. Non-Cryst. Solids **1023**, (2002).
- [3] M.A. Urena, A.A. Piarristeguy, M. Fontana, B. Arcondo, Solid State Ionics **176**, 505, (2005).

- [4] V. Zima, T. Wagner, Mil. Vlcek, L. Beneš, S.O. Kasap, M. Frumar, J. Non-Cryst. Solids **159**, (2003).
- [5] S.R. Elliot, A.T. Steel, J. Phys. C: Solid State Phys. **20**, (1987).
- [6] M.V. Šiljegović, S.R. Lukić, F. Skuban, D.M. Petrović, M. Slankamenac, Journal of Optoelectronics and Advanced Materials **11**, 12, (2009).
- [7] M. V. Šiljegović, D. D. Štrbac, Lj. R. Đaćanin, I. O. Gut, The Third Scientific-Technical Meeting, Book of Abstracts **59**, InterRegioSci 2008.
- [8] P. Debye, *Polar Molecules* (Chapter V), New York, (1929).
- [9] V.S. Edelman, Sov. Fiz. Usp. **20**, 819, (1977).
- [10] J.C. Phillips, J. Non. Cryst. Solids **55**, 179, (1983).
- [11] M. Kastner, D. Adler, H. Fritzche, Phys. Rev. Lett. **37**, 22, (1976).
- [12] O.S. Panwar, M. Radharishna, K.K. Srivastava, K.N. Lakshminarayan, Phil. Mag. B **41**, 253, (1980).
- [13] D.K. Goel, C.P. Singh, R.K. Shukla, A. Kumar, J. Mater. Sci. **35**, 1017, (2000).
- [14] P. W. Anderson, Phys. Rev. Lett. **34**, 953, (1975).
- [15] N. Thoge, Y. Yamamoto, T. Minami, M. Tanaka, J. Appl. Phys. Lett. **34**, 640, (1979).
- [16] K.L. Bhatia, G. Parthasarthy, A. Sharma, E.S.R. Gopla, Phys. Rev. B **38**, 6342, (1988).
- [17] P. Nagels, L. Tichy, A. Triska, H. Ticha, J. Non. Cryst. Solids **59 & 60**, 1015, (1983).
- [18] J.M. Stevels, *The electrical properties of glasses*, 350, (1975).
- [19] R. Arora and A. Kumar, J. Mater. Sci. Lett. **9**, 348, (1990).
- [20] D.R. Goyal, S. Walker, K.K. Srivastava, Phys. Stat. Sol. **64**, 351, (1981).
- [21] M. Zulfequar, A. Kumar, J. Electrochem. Soc. **136**, 1099 (1989).
- [22] S. Srivastava, N. Mehta, C.P. Singh, R.K. Shukla, A. Kumar, Physica B **403**, (2008).
- [23] Satish Kumar, M. Husain, M. Zulfequar, Physica B **387**, (2007).
- [24] I.O. Guth, D.M. Petrović, M. Šiljegović, S.R. Lukić, Journal of Optoelectronics and Advanced Materials **9**, 1694-1698, (2007).
- [25] K. S. Cole and R. H. Cole: J. Chem. Phys. **9**, 841, (1941).
- [26] B. Tareev, *Physics of dielectric materials*, Mir Publishers, Moskow, (1975).
- [27] M.E. Borisova, S.N. Kajkov, *Fizika dielektrikov*, Izd. Mir, Moskva, (1980).
- [28] H. Eyring, J. Chem. Phys. **4**, 283, (1936).

Calculation of Single-layer and Multilayer Chalcogenide Films Refractive Index using Cheremukhins Method

M.V. Šiljegović¹, S.R. Lukić-Petrović^{1*}, Lj.R. Đaćanin¹, D.D. Štrbac²

¹*University of Novi Sad, Department of Physics, Faculty of Sciences,
Trg Dositeja Obradovica 4, 21000 Novi Sad, Serbia*

²*University of Novi Sad, Faculty of Technical Sciences, Novi Sad, Serbia*

Received: December 23, 2009

Abstract

This paper presents the results obtained by using Cheremukhins model to calculate the refractive index and its dispersion for single-layer As_2S_3 and $\text{Se}_{60}\text{Te}_{40}$ thin-film and multilayer $\text{As}_2\text{S}_3/\text{Se}_{60}\text{Te}_{40}$ film. Thin films were deposited under vacuum on glass substrates by thermal evaporation technique, from previously synthesized bulk samples.

It was found that the refractive index shows normal dispersion behavior, with high values in the vicinity of the absorption edge. Refractive index values for single-layer films As_2S_3 and $\text{Se}_{60}\text{Te}_{40}$, are higher than 2 for the whole spectral range, while the values for multilayer film $\text{As}_2\text{S}_3/\text{Se}_{60}\text{Te}_{40}$ are slightly lower.

Key words: chalcogenides, refractive index, thin films, Cheremukhins model

1. Introduction

Multicomponent chalcogenide glasses are widely used in the field of semiconducting techniques. The application areas of these glasses are: energy management, thermography, temperature monitoring, electronic circuit detection, laser technique and IR-spectroscopy, as well as high-resolution optics in night image technique. Most chalcogenide glasses are opaque in the visible region, with the exception of some sulfide glasses, which are dark red. They transmit from approximately $1\ \mu\text{m}$ to infrared wavelengths longer than those of oxide or fluoride glasses. In the infrared region, transparency is restricted by the vibrations of molecules, atoms and ions in the glass network. The long-wavelength limit is therefore often referred to as the vibrational or multiphonon edge. The absorption results from the interaction of the incident radiation with the vibrational modes of the glass structure, which can cause changes of the dipole moment. Glasses containing heavier ions transmit longer wavelengths. Sulfide glasses are transparent up to $12\ \mu\text{m}$, selenide glasses up to $15\ \mu\text{m}$, and telluride glasses transmit up to $20\ \mu\text{m}$. Thin films deposited from the chalcogenide glasses are applicable in opto- and micro-electronics for different purposes - electrical switches, data recording, protective, passivity and optical coatings [1,2]. The use

*Corresponding author: svetlana@df.uns.ac.rs

of the chalcogenides as protective layers of some elements in the optoelectronics, as well as an active component in the preparation of electronic elements requires the knowledge of the magnitude of refractive index in the spectral range where these materials exhibit normal dispersion (i.e. lowering of the refractive index values at higher wavelengths).

The aim of this work was to determine the refractive index as an important physical parameter of chalcogenides for their applications. Because of large values of the refractive index of chalcogenide glasses, the determination of this physical parameter and its spectral dependence requires, as a rule, non-standard methods [3]. This paper presents the analysis of characteristics of three thin chalcogenide films. Two of them, As_2S_3 and $\text{Se}_{60}\text{Te}_{40}$, are single-layer films, and $\text{As}_2\text{S}_3/\text{Se}_{60}\text{Te}_{40}$ is a multilayer film.

2. Description of the Experiment

Thin films were deposited under vacuum on glass substrates by thermal evaporation technique (Fig. 1), from the previously synthesized bulk samples. Bulk glasses were synthesized in cascade regime from high purity elemental components (99.998 %) and air quenched according to the empirically defined cascade regimes. The amorphous character of the obtained samples was confirmed by the methods of X-ray diffraction and polarization microscopy.

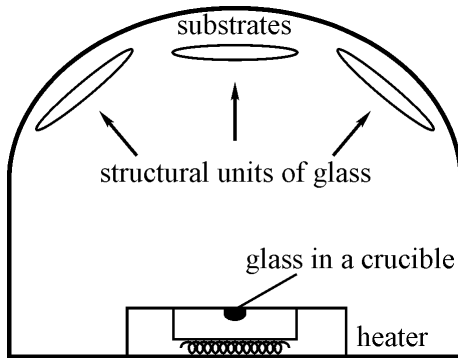


Figure 1. Scheme for thermal evaporation technique.

Condensation was carried out on the transparent substrates with the known index of refraction (glass K-8, $n_p = 1.516$), kept at room temperature. Film thickness during deposition was controlled by optical method on the basis of the interference of reflected laser beam.

Transmission spectra of obtained samples and substrates were recorded on a double-beam UV/VIS/NIR Perkin-Elmer spectrophotometer, model Lambda-950. The spectrophotometer was set with slit width of 1 nm. All optical measurements were performed at room temperature.

3. Results and Discussion

The refractive index values were determined by interference maxima appearing in the optical transparency spectra of obtained film samples. Calculation and discussion of this physical parameter were performed using Cheremukhins model [4]. Transmission of each film is defined by the relative method, with a glass as a reference sample. Figures 2 and 3 shows representative transmission spectra of single-layer and multilayer films.

On the basis of the recorded spectra, a very high transparency can be established for the As_2S_3 and $\text{Se}_{60}\text{Te}_{40}$ films and quite low transparency of the $\text{As}_2\text{S}_3/\text{Se}_{60}\text{Te}_{40}$ film, as well as the shift of the absorption edge to higher wavelengths in case of the multilayer film $\text{As}_2\text{S}_3/\text{Se}_{60}\text{Te}_{40}$ compared to the single-layer films As_2S_3 and $\text{Se}_{60}\text{Te}_{40}$.

Cheremukhin's method allows the determination of refractive index from the coordinates of peak's minima (T_{\min}) and maxima (T_{\max}) in the transmission spectra of investigated films.

$$n = \frac{1}{2} \left\{ (n_s + 1) \left[\sqrt{C} - \sqrt{C - \frac{4n_s}{(n_s + 1)^2}} \right] \right\}, \quad (1)$$

where $C = \sqrt{\frac{T_{\max}}{T_{\min}}}$, n - refractive index of thin film, n_s - refractive index of the substrate on which the film is deposited by thermal treatment.

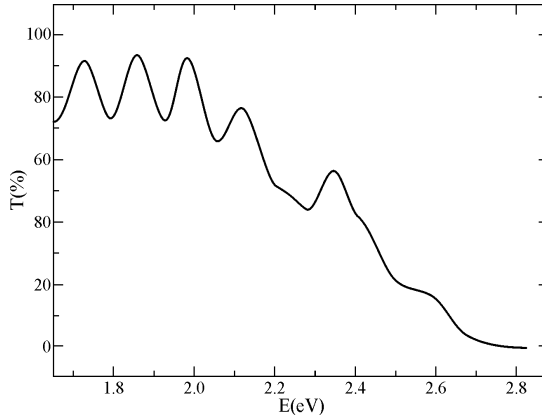


Figure 2. Transmission spectra of film As_2S_3 .

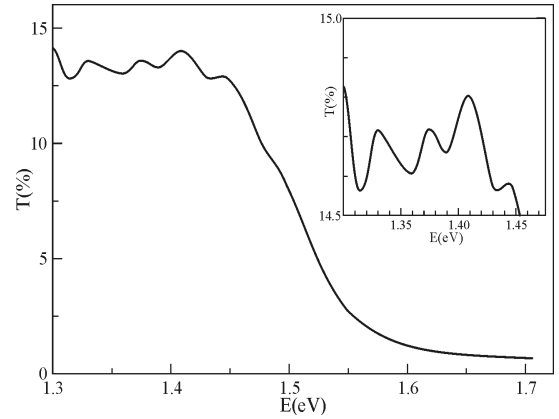


Figure 3. Transmission spectra of film $\text{As}_2\text{S}_3/\text{Se}_{60}\text{Te}_{40}$, insert part refers to magnified spectral range in which transmission maxima occurs.

The results obtained are presented in Fig. 4-6.

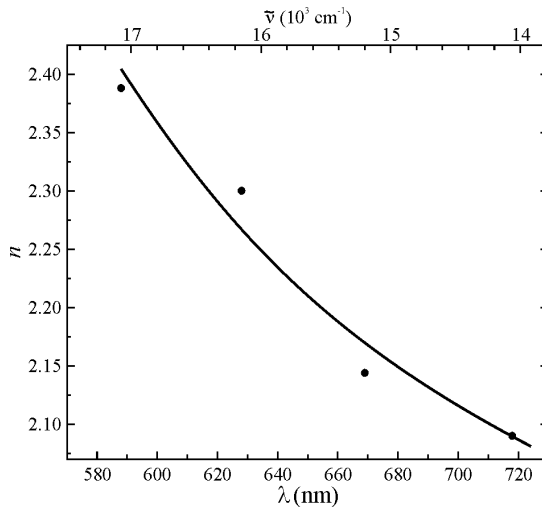


Figure 4. Refractive index dispersion of As_2S_3 film.

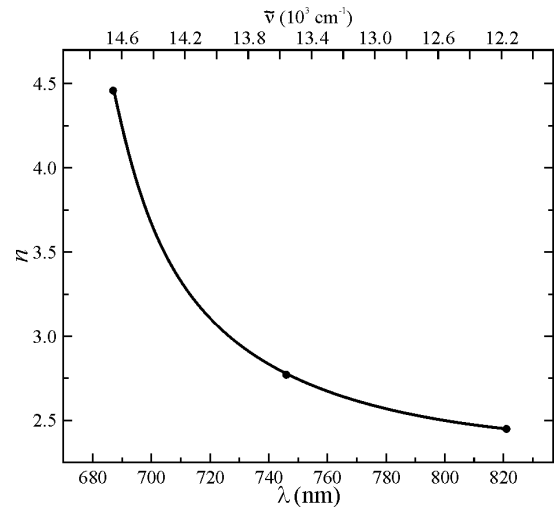


Figure 5. Refractive index dispersion of $\text{Se}_{60}\text{Te}_{40}$ film.

Studies of the refractive index behavior of these chalcogenide films at room temperature in the wavelength range from the absorption edge to 1000 nm showed that these amorphous samples are characterized by normal dispersion.

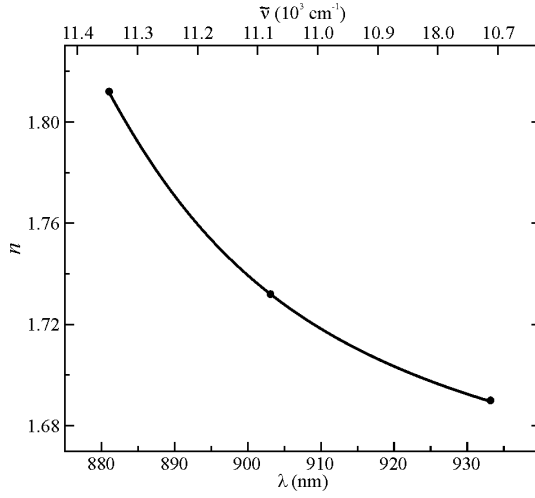


Figure 6. Refractive index dispersion of $\text{As}_2\text{S}_3/\text{Se}_{60}\text{Te}_{40}$ film.

films of different composition is graphically presented in Figs. 7-9.

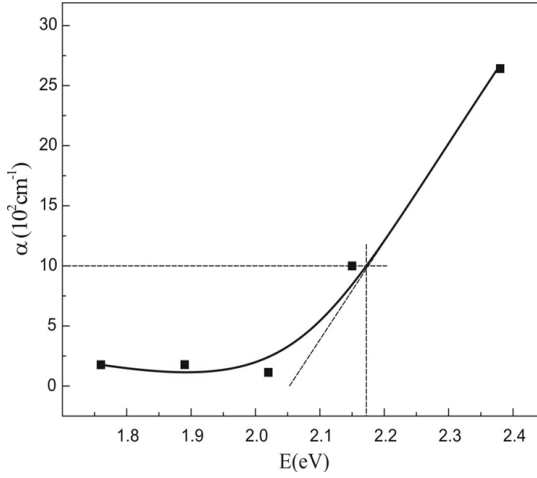


Figure 7. Absorption coefficient dispersion of As_2S_3 film.

These films, and especially the single-layer As_2S_3 and $\text{Se}_{60}\text{Te}_{40}$ thin films, exhibited very high values of the refractive index in the vicinity of the absorption edge.

Also, the transparency spectra allowed the determination of the corresponding absorption coefficients using the following relation:

$$\alpha = \frac{1}{d} \ln \frac{(1 - R_1)(1 - R_2)(1 - R_3)}{T_S}, \quad (2)$$

where $T_s = \sqrt{T_{\max} T_{\min}}$, R_1 -refractive index at the air-film interface, R_2 -refractive index at the film-substrate interface, R_3 -refractive index at the substrate-air interface.

Dispersion of this parameter for three

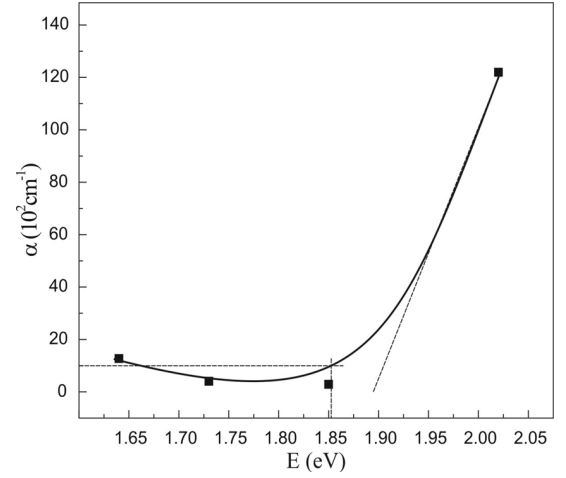


Figure 8. Absorption coefficient dispersion of $\text{Se}_{60}\text{Te}_{40}$ film.

The extrapolation of the linear parts of the curves showing the dependence $\alpha = \alpha(\lambda)$ allowed the determination of the absorption edge and optical bandgap.

Optical bandgap can be defined in two ways. The first applies Stuke's method [5], which consists of readouting the energy value from the graph $\alpha = f(h\nu)$ for the absorption coefficient value $\alpha = 10^4 \text{ cm}^{-1}$. The other method is the extrapolation of the linear part of the curve $\alpha = f(h\nu)$. Eg defined this way is by 0.1 – 0.2 eV lower than the value calculated by Stuke's method [6]. In our case, both methods are used for the first two films.

It has to be noted that when using Stuke's method we chose the value of 10^3 cm^{-1} for absorption coefficient, which is correct in the case of strong absorption. Stuke's method was not applied on multilayer film since it was not possible to read the corresponding energy value from the curve. The results are presented in Table 1.

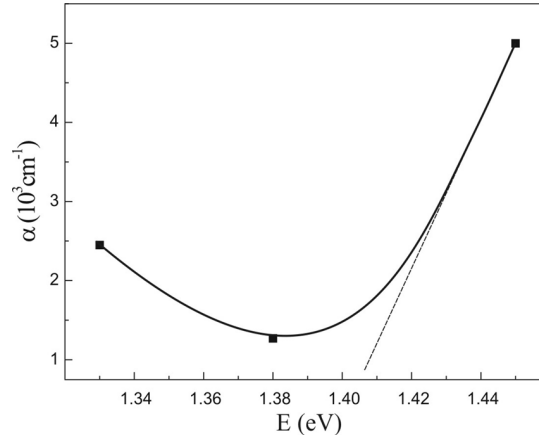


Figure 9. Absorption coefficient dispersion of $\text{As}_2\text{S}_3/\text{Se}_{60}\text{Te}_{40}$ film.

Table 1. Values of optical bandgap for investigated samples.

samples	Optical bandgap E_g [eV]	
	Stuke's method	Extrapolation method
As_2S_3	2.053(25)	2.172(25)
$\text{Se}_{60}\text{Te}_{40}$	1.852(25)	1.895(25)
$\text{As}_2\text{S}_3/\text{Se}_{60}\text{Te}_{40}$	-	1.397(5)

4. Conclusion

To sum up, the determined transparency of As_2S_3 and $\text{Se}_{60}\text{Te}_{40}$ films was very high, while the transparency of $\text{As}_2\text{S}_3/\text{Se}_{60}\text{Te}_{40}$ film was quite low, and the absorption edge was shifted to higher wavelengths in the case of the multilayer film $\text{As}_2\text{S}_3/\text{Se}_{60}\text{Te}_{40}$ compared to the single-layer films As_2S_3 and $\text{Se}_{60}\text{Te}_{40}$.

We found that the refractive index shows normal dispersion behavior and high values in the vicinity of the absorption edge. Refractive index values for single-layer films As_2S_3 and $\text{Se}_{60}\text{Te}_{40}$ are higher than 2 for the whole spectral range, while the values for multilayer film $\text{As}_2\text{S}_3/\text{Se}_{60}\text{Te}_{40}$ are slightly lower. Therefore, we might conclude that this film can not be treated as a simple summation of single layers [7,8] and that the experimental curves should be analyzed on the basis of other theory models, and not by Cheremuhin's method.

It is shown that the values of optical bandgap depend on the determination method used. The values derived for the optical bandgap from 1.40 eV–2.17 eV for these films are typical for semiconductor materials.

Acknowledgments

The work is done as part of the Project No. 141026 "Amorphous and Nanostructural Chalcogenides", supported by the Ministry of Science and Technological Development, Republic of Serbia and Project "Technology of obtaining and characterization of disordered semiconductors" supported by the Provincial Secretariat of Science and Technological Development, Autonomous Province of Vojvodina.

References

- [1] A. Madan, M.P. Shaw, *The Physics and Applications of Amorphous Semiconductors*, Academic Press, Inc., Boston - San Diego, 1988.
- [2] S.V. Svechnikov, V.V. Khiminets, N.I. Dovgoshey, *Non-crystalline Multinary Chalcogenides and Chalcohalides and Their Application in Optoelectronics*, Naukova Dumka, Kiev, 1992.
- [3] S. Lukić, D. Petrović, *Complex noncrystalline chalcogenides*, (in Serbian, University of Novi Sad, Faculty of Sciences, Novi Sad, 2002).
- [4] G.S. Cheremukhin, B.V. Kirienko, E.K. Gurdin, *Optiko-mekhan. Prom.*, **6**, 13, 1976.
- [5] J.J. Stuke, *Journal of Non-Crystalline Solids*, **4**, 1, 1970.
- [6] N.F. Mott, E.A. Davis, *Electronic Processes in Non-Crystalline Materials*, Clarendon Press, Oxford, 1979.
- [7] V. Takatsa, I. Vojnarovichb, V. Pinzenikb, I. Mojzecs, S. Kokenyesia, K.S. Sangunni, *Journal of Physics and Chemistry of Solids* **68**, 2007.
- [8] I. Vojnarovych, V. Takach, V. Cheresnya, V. Pynzenik, I. Makauz, S. Chernovich, *Physics and Chemistry of Solid State* **8**, 4, 2007.

Journal of Research in Physics

INFORMATION FOR CONTRIBUTORS

This Journal is devoted to the publication of original papers in **fundamental and applied physics**. The papers are in principle Articles, while Review Articles will be published by invitation only.

Contributors should send their manuscripts to Professor M. Škrinjar, Editor, Department of Physics, Faculty of Sciences, University of Novi Sad, Trg Dositeja Obradovića 4, 21000 Novi Sad, Serbia. (Fax #: +381-(21)-459-367; E-mail: jresphys@df.uns.ac.rs).

All manuscripts must be submitted in English. Manuscripts should be submitted in duplicate and should be typewritten and double spaced with wide margins. Only one side of each sheet should be used.

Manuscripts should consist of the title, followed by author(s) name(s) and adresse(s), abstract, key words, body of the text and the list of the references. Authors should *not* include references in Abstracts.

References must be numbered in the order in which they are referred to in the text: e.g. S. Wagner [1] or [1]. In the text, such abbreviations as Ref. [4] or Refs. [7-10] may be used.

The full references should be listed in the numerical order of citation in the text at the end of the article. Examples:

1. S. Autler and C. H. Townes, Phys. Rev. A **10**, 489 (1982). – for articles
2. E. U. Shirley, *The Theory of Molecules*, p. 399, (The University Press, Cambridge, 1954). – for books
3. C. E. Moore, "Selected Tables of Atomic Spectra", NSRDS-NBS3, Setion 5, National Bureau of Standards, Washington, DC 20025 (1975). – for reports.

Tables and figures should be sent with the paper on the separate pages. All photographs, graphs, and diagrams should be numbered consecutively. The legends should be typed on a separate page at the end of the article. The author's name, the figure number, and an indication of its proper orientation should be written on the back of each figure.

Line drawings must be submitted in camera-ready form and should be drawn in india ink on stiff white paper or printed on quality laser printer. The letters and symbols should be drawn so as to be clearly legible when reduced.

Authors are asked to suggest at least three referees who may revise their manuscript.

Page proofs will be sent to the author (or the first-mentioned author in a paper of multiple authorship) for checking. **Corrections to the proofs must be restricted to printer's errors.** Authors are particularly requested to return their corrected proofs as quickly as possible. Please note that **authors are urged to check their proofs carefully before return, since late corrections cannot be guaranteed for inclusion in the printed journal.**

The first-named author of each paper will receive 25 reprints free of charge.

Journal of Research in Physics

Volume 33 Number 1 December 2009

CONTENTS

Dragan R. Todorović	Origination of the Davydov's Soliton in the Linear Polymer Chain	1
M. Pavkov-Hrvojević, M. Pantić, S. Radošević, M. Rutonjski, D. Kapor	Magnetic Excitations of Ferromagnetic Semiconductor Superlattices	13
S. Djurović, I. Savić	Correction of the H_{β} Spectral Line Profile for the Influence of the Neighbour Hydrogen Lines	21
D.Ž. Obadović, M. Stojanović, S. Jovanović-Šanta, J. Nikolov, D. Lazar, M. Cvetinov, A. Vajda, N. Éber	Phase Transition Temperature Shifts in Binary Cholesteric Liquid Crystalline Mixtures Doped with some Chiral Nonmesogenic Additives	29
Nataša Lalović, Agneš Kapor, Željka Cvejić, Sonja Skuban, Srđan Rakić, Stevan Jankov	Dielectric Properties of Molecular Inclusion Complex of β -cyclodextrin and iron fumarate	37
N. Jovančević, M. Krmar, J. Slivka, D. Mrdja, I. Bikit	Deuterium Production as a Possible Tool for Estimation of the Thermal Neutron Fluence in the Low-background Ge-detector	49
M.V. Šiljegović, S.R. Lukić-Petrović, M. Slankamenac, R.V. Kisić, A.S. Tver'yanovich	Analysis of Some Dielectric Parameters of the $\text{Bi}_6(\text{As}_2\text{S}_3)_{94}$ Glass	55
M.V.Šiljegović, S.R. Lukić-Petrović, Lj.R. Đačanin, D.D. Štrbac	Calculation of Single-layer and Multilayer Chalcogenide Refractive Index using Cheremukhin's Method	63